# Damped Gravity Waves, Weak Temperature Gradients, and Tropical Deep Convection

Ángel F. Adames Corraliza[1] , Víctor C. Mayta[1] , Fiaz Ahmed[3] , Brandon O. Wolding[2] , and Kathleen A. Schiro[4]

[1] *Department of Atmospheric and Oceanic Sciences, University of Wisconsin, Madison, Wisconsin*
[2] *Department of Atmospheric and Oceanic Sciences, University of California, Los Angeles, Los Angeles, California*
[3] *Physical Sciences Division, NOAA/Earth System Research Laboratory, Boulder, Colorado*
[4] *Department of Environmental Sciences, University of Virginia, Charlottesville, Virginia*

***This manuscript was submitted on 9/30/2024 and has not been peer reviewed.***

ABSTRACT: The "damped gravity wave" (DGW) approximation occurs when convective momentum dissipation is balanced by the pressure gradient force of convectively forced gravity waves. While this balance has been used to parameterize large-scale lifting in limited-domain models of tropical deep convection, its applicability to observed phenomena has not been carefully examined. A scale analysis indicates that DGW balance can occur in tropical cloud clusters occurring in low shear environments, with horizontal scales of ~ 100 km or greater and timescales of a day. The DGW balance is then used to explain three well-known properties of tropical deep convection. First, DGW balance implies that the average mesoscale vertical velocity in cloud clusters will be closer to first baroclinic, with second baroclinic motions contributing a smaller fraction of the total ascent. The first baroclinic mode is dominant because gravity waves and momentum diffusion induce a nonlocal velocity response to buoyancy, making ascent over regions of negative buoyancy possible. Second, a combination of the weak temperature gradient (WTG) and DGW balances yields a form of convective quasi-equilibrium, with adjustment timescales comparable to those previously estimated. Third, the use of WTG-DGW approximations in an entraining plume model reproduces the empirical precipitation-buoyancy relationship from Ahmed and Neelin. The sensitivity of precipitation to mean CAPE is interpreted as a small excursion from the zero buoyancy approximation where the undilute buoyancy and dilution by entrainment nearly, but not completely, cancel. Overall, these results support viewing cloud clusters as a coupling between deep convection and gravity waves.

SIGNIFICANCE STATEMENT: Large regions of tropical thunderstorms, referred to as cloud clusters, can dissipate winds in the troposphere. The cloud clusters also force large atmospheric ripples that are known as gravity waves. In this study we show that when we combine these two consequences of cloud clusters we can explain three features of the tropics. First, it explains why the predominant form of vertical motion consists of deep ascent throughout the troposphere. Second, it shows that cloud clusters achieve an equilibrium between the instability that amplifies them and the dissipation they create at timescales that agree with previous work. Third, it explains why tropical precipitation picks up very rapidly once a specific threshold is met. These results support viewing cloud clusters as a coupling thunderstorms and gravity waves.

## 1. Introduction

A major feature of the tropics is the prevalence of large regions of deep convection. While individual cumulonimbus are usually on the scale of tens of kilometers or less, they can also organize into much larger cloud clusters (Chang 1970; Zangvil 1975) (see Fig. 1). These cloud clusters can be comprised of multiple cumulonimbus clouds and/or may include one or multiple mesoscale convective systems (MCSs). These regions of deep convection can be further organized by large-scale weather systems such as convectively coupled waves and the Madden-Julian Oscillation, providing an important source of predictability (Dias et al. 2018; Janiga et al. 2018; Kim et al. 2018). Collectively, cloud clusters play a critical role in global energy transport, and their rainfall affects the livelihood of nearly half of the global population (Schumacher et al. 2004; Bischoff and Schneider 2014; Edelman et al. 2014).

Observations have shown that both disorganized and organized convection exhibit deep inflow profiles that mix free-tropospheric air into updrafts (Kingsmill and Houze 1999; Schumacher et al. 2015; Schiro et al. 2018). These deep profiles are dominated by the so-called "first baroclinic mode" in vertical velocity. In the first baroclinic mode, ascent increases from the surface, peaks in the mid-troposphere, and decreases until vanishing near the tropopause. This vertical velocity profile accounts for nearly 80% of the large-scale (>100 km in length) vertical velocity variance in the tropics (Tung et al. 1999; Back et al. 2017; Inoue et al. 2020). While it's dominance can be explained by invoking convective quasi-equilibrium (Emanuel et al. 1994), the details on how this dominance comes about have not been thoroughly examined.

The mixing that is associated with deep inflow makes convection sensitive to the concentration of moisture in the

*Corresponding author*: Ángel F. Adames Corraliza, angel.adamescorraliza@wisc.edu

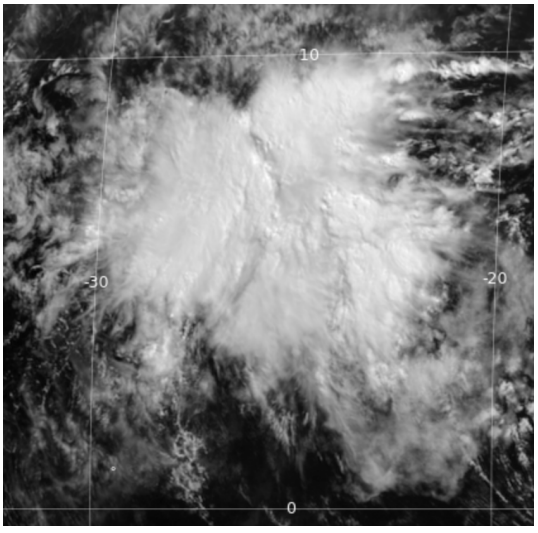


FIG. 1. Meteosat-10 635 nm image of a cloud cluster over the eastern north Atlantic that occurred on June 12, 2024.

lower free troposphere (Ahmed and Neelin 2018; Schiro et al. 2018). This sensitivity is well captured if the convection is treated as an entraining plume whose buoyancy is determined by the thermodynamic properties of the boundary layer and the overlying free troposphere (Brown and Zhang 1997; Ahmed and Neelin 2018; Schiro and Neelin 2019a; Wolding et al. 2022). Application of this plume buoyancy framework to observations and reanalysis reveals that rainfall increases steeply and quasi linearly after some critical buoyancy value is exceeded (Ahmed and Neelin 2018; Ahmed et al. 2020; Adames et al. 2021). While this linear relationship has been used to parameterize convection in simple models of tropical motions (Ahmed et al. 2020, 2021; Adames et al. 2021; Ahmed 2021), we still lack an explanation for it that is based on first principles.

It is well-known that tropical precipitation is directly related to large-scale vertical motions via the weak temperature gradient approximation (Sobel and Bretherton 2000; Sobel et al. 2001). However, the details as to how buoyancy is related to these two are less clear and require a close examination of the horizontal and vertical momentum equations. Romps (2012b) suggested that the leading-order balance in the horizontal momentum equations in convecting regions is between the pressure gradient force and frictional dissipation. This balance is sometimes referred to as "antitriptic balance" (Bluestein 1992), the "weak pressure gradient" (WPG) approximation (Romps 2012b), or the "damped gravity wave" (DGW) approximation (Kuang 2008; Blossey et al. 2009; Wang et al. 2013). In this study we will refer to it as DGW balance. In this balance, the large-scale winds steadily flow down the pressure gradient of the convective region, as in a viscous fluid.

DGW balance has been used as a way to parameterize large-scale vertical motions in regional cloud-permitting models (Romps 2012a; Wang et al. 2013; Daleu et al. 2015, 2016; Singh and Neogi 2022). The results of these studies indicate that it can reasonably simulate large-scale anomalies in vertical motion and buoyancy. Aside from this application, the possibility that tropical convecting regions are in DGW balance has received little attention. This may be partly due to the fact that antitriptic flow is considered to be a rare occurrence in the troposphere (Bluestein 1992), even though many studies have suggested that cumulus momentum transports in unorganized deep convection approximately act as friction (Mapes and Wu 2001; Tung and Yanai 2002; Blossey et al. 2009; Kuang 2011; Romps 2014).

In this study, we will examine whether a form of the DGW appproximation where the friction comes from eddy diffusion of momentum by convection can be used to better understand regions of deep convection such as tropical cloud clusters (Fig. 2). Specifically, we will seek to answer the following questions:

1. Under what conditions is the DGW approximation valid?
2. Can the DGW approximation explain the preponderance of the first baroclinic mode in vertical velocity in the tropics?
3. Can the DGW approximation explain the linear relationship between buoyancy and rainfall?

This study is structured as follows. Data and methods are discussed in the next section. The idea that convective momentum transports act diffusively along with the basic equations is introduced in section 2. Section 3 shows how DGW balance can occur through the application of scale analysis. In Section 5 we employ a simple model to better understand the adjustment towards and the consequences of DGW balance on deep convection. In Section 6 we treat cloud clusters as entraining plumes and show that the DGW and WTG approximations can explain the precipitation-buoyancy relation. We summarize this work and offer conclusions in Section 7.

## 2. Basic equations

We will begin our analysis by considering the basic equations averaged over a domain that is on the order $\sim 100$ km, a scale typically used to characterize the tropical mesoscale (Fig 3a; Houze 2004). Domain-averaged variables will be denoted with an overline (e.g. $\overline{u}$) and double primes denote deviations from the domain mean (e.g. $u''$). These deviations will correspond to the smaller-scale elements that exist within the active convection (see Fig. 3b) that are of a horizontal scale $\ll 100$ km.

Romps (2014) showed that convective momentum transport in unorganized convection acts as a momentum diffusion for the leading baroclinic modes in vertical motion

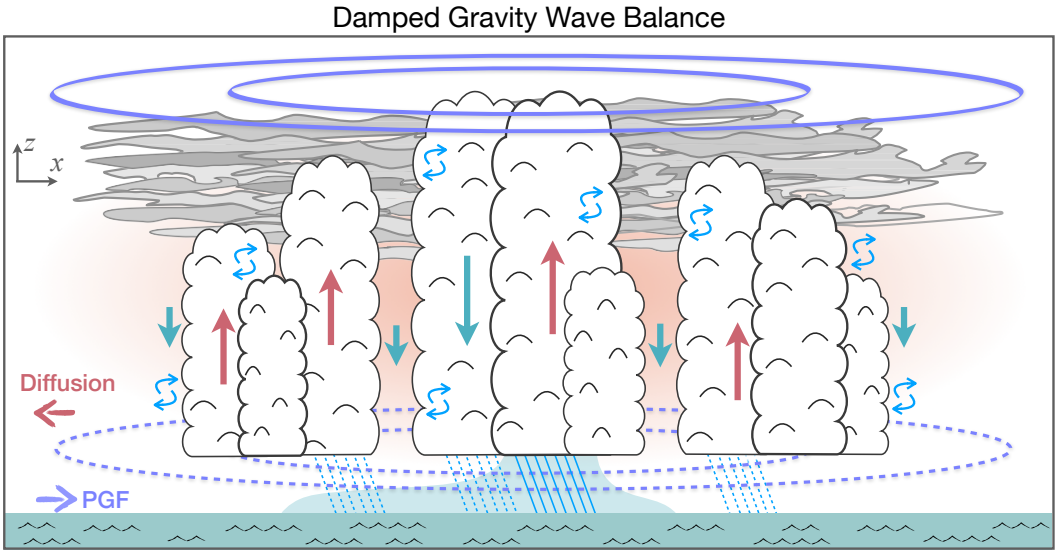


FIG. 2. Schematic showing DGW balance (Eq. (22a)) in a tropical cloud cluster. Purple contours show the anomalous pressure. The blue curved arrows denote the subdomain-scale eddies. Red and cyan arrows denote small-scale updrafts and downdrafts, respectively. The governing forces in the horizontal momentum equations are shown as arrows in the lower-left corner.

TABLE 1. The main variables and definitions used in this study.

| *Var.* | *Description* | *Units* |
|---|---|---|
| $p$ | Pressure | Pa |
| $T$ | Temperature | K |
| $\rho$ | Density | $s^{-1}$ |
| $B$ | Buoyancy | m $s^{-2}$ |
| $N$ | Brünt-Vaisala frequency | $s^{-1}$ |
| $f$ | Planetary vorticity | $s^{-1}$ |
| $\mathbf{v}$ | Horizontal vector wind | m $s^{-1}$ |
| $w$ | Vertical wind | m $s^{-1}$ |
| $M_u$ | Convective updraft mass flux | $m^{-1}$ |
| $\varepsilon$ | Effective entrainment rate | $m^{-1}$ |
| $\mu_c$ | Eddy exchange coefficient | kg $m^{-1}$ $s^{-1}$ |
| $Q_1$ | Apparent heating | W $s^{-1}$ |
| $Q$ | Apparent buoyancy source | m $s^{-3}$ |
| $c$ | Gravity wave phase speed | m $s^{-1}$ |
| $\tau_\epsilon$ | Convective dissipation timescale | s |
| $\tau_g$ | Gravity wave adjustment timescale | s |
| $\tau_r$ | Convective response timescale | s |

(see Appendix A), allowing us to write the subdomain-scale momentum fluxes as:

$$\overline{\rho}\,\overline{u''w''} = -\mu_c \frac{\partial \overline{u}}{\partial z} \tag{1}$$

where $\rho$ is the density, $\overline{u''w''}$ is the turbulent vertical zonal momentum flux, $\mu_c$ is the eddy exchange coefficient, and $\overline{u}$ is the domain-mean zonal wind. As in the mixing length hypothesis, $\mu_c$ is defined as a mass flux ($M_u$) that is characteristic of the small-scale updrafts (such as those shown in Fig. 3b) multiplied by the mean free path of parcels. This mean free path is the inverse of the effective fractional entrainment rate of the small-scale updrafts ($\varepsilon$):

$$\mu_c = \frac{M_u}{\varepsilon}. \tag{2}$$

The term $\varepsilon$ actually accounts for the fractional entrainment and the horizontal pressure gradient force between updrafts and the environment. For simplicity, we assume that its properties are similar to the entrainment rate, which is largest over the boundary layer and tends to decrease with height (Romps 2010; Hannah 2017; Xu et al. 2021). In contrast, $M_u$ increases rapidly in the first few kilometers above the surface, and slowly decreases throughout the rest of the troposphere. These results suggest that $\mu_c$ can be treated as independent of height to qualitatively represent the horizontal accelerations driven by subdomain-scale updrafts and downdrafts. These assumptions are similar to those made by Romps (2014).

After making these assumptions and approximations we write the momentum, mass continuity and thermodynamic equations as:

$$\frac{\overline{D}\overline{\mathbf{v}}}{Dt} = -\frac{1}{\overline{\rho}}\nabla_h \overline{p}' - f\mathbf{k}\times\overline{\mathbf{v}} + \frac{\mu_c}{\overline{\rho}}\frac{\partial^2 \overline{\mathbf{v}}}{\partial z^2} \tag{3a}$$

$$\frac{\overline{D}\overline{w}}{Dt} = -\frac{1}{\overline{\rho}}\frac{\partial \overline{p}'}{\partial z} + \overline{B} + \frac{\mu_c}{\overline{\rho}}\frac{\partial^2 \overline{w}}{\partial z^2} \tag{3b}$$

$$\nabla_h \cdot \overline{\rho}\overline{\mathbf{v}} = -\frac{\partial \overline{\rho w}}{\partial z} \tag{3c}$$

$$C_p \frac{\overline{D}\overline{T}}{Dt} + \overline{w}g = Q_1 \tag{3d}$$

where

$$\frac{\overline{D}}{Dt} = \frac{\partial}{\partial t} + \overline{u}\frac{\partial}{\partial x} + \overline{v}\frac{\partial}{\partial x} + \overline{w}\frac{\partial}{\partial z} \tag{4}$$

is the domain-averaged material derivative, $\mathbf{v}$ is the horizontal vector wind, $w$ is the vertical velocity, $\rho$ is the density, $p'$ is the pressure perturbation from global hydrostatic balance, $\nabla_h$ is the horizontal gradient,

$$\overline{B} = g\frac{T'}{T_e} \tag{5}$$

is the buoyancy, defined as the temperature deviation from the value that satisfies hydrostatic balance ($T_e$), where $T' = \overline{T} - T_e$,

$$Q_1 = \overline{Q}_c + \overline{Q}_r - \frac{\partial \overline{w''s''}}{\partial z} \tag{6}$$

is the apparent heating rate (Yanai et al. 1973), where $\overline{Q}_c$ is the domain-mean latent heat release in convection, $\overline{Q}_r$ is the radiative heating, an $\overline{w''s''}$ is the subgrid-scale flux of dry static energy ($s = C_pT + gz$).

It will be convenient to write Eq. (3d) in terms of buoyancy. We do this by multiplying Eq. (3d) by $g(C_pT_e)^{-1}$, yielding the following

$$\frac{\partial \overline{B}}{\partial t} + \overline{\mathbf{v}} \cdot \nabla_h \overline{B} + \overline{w}N^2 = \overline{Q} \tag{7}$$

where

$$N = \sqrt{\frac{g}{C_pT_e}\frac{\partial s}{\partial z}} \tag{8}$$

is the Brünt-Vaisala frequency, and

$$\overline{Q} = \frac{gQ_1}{C_pT_e} \tag{9}$$

is the diabatic buoyancy source. From here on, the overlines will be dropped and variables will correspond to ~100 km domain averages unless otherwise stated.

## 3. Scale analysis

We will now perform a scale analysis on Eqs. (3a)-(3d) in order to understand when DGW balance is valid. The independent variables scale as:

$$(x, y) = \mathrm{L}(\hat{x}, \hat{y}) \qquad z = \mathrm{H}\hat{z} \qquad t = \tau\hat{t} \tag{10}$$

while the zonal, meridional and vertical winds scale as:

$$(u, v) = \mathrm{U}(\hat{u}, \hat{v}) \qquad w = \mathrm{W}\hat{w}. \tag{11}$$

The scales U and W can be related to one another by scaling Eq. (3c), yielding:

$$\mathrm{W} = \frac{\mathrm{UH}}{\mathrm{L}}. \tag{12}$$

To keep the discussion in this section as simple as possible, we assume that the Eulerian tendency of momentum and the advection terms are of comparable magnitude, implying that:

$$\tau \sim \frac{\mathrm{L}}{\mathrm{U}}. \tag{13}$$

Note that in using this scaling we are assuming that the irrotational component of the horizontal flow is comparable or larger than its non-divergent component. This scaling implies that the Rossby number $\mathrm{Ro} = (\tau\zeta_a)^{-1}$ (Raymond et al. 2015), where $\zeta_a = f + \zeta$ is the absolute vorticity, is of order unity or greater.

Since we are interested in the conditions in which the DGW approximation is satisfied, we will scale the pressure gradient force as being of the same order as the vertical diffusion of horizontal momentum. For this, it will be convenient to define the scaling of $M_u$ as:

$$M_u \sim \rho\sigma \mathrm{W}_u \tag{14}$$

where $\sigma$ is the area fraction of the domain occupied by updrafts (Yanai et al. 1973), and $\mathrm{W}_u$ is a characteristic velocity of the subdomain-scale updrafts. With this definition, the scale of the pressure anomaly is written as:

$$p' \sim \frac{\rho \mathrm{LU}}{\tau_\varepsilon}\hat{p}'. \tag{15}$$

where

$$\tau_\epsilon = \frac{\rho \mathrm{H}^2}{\mu_c} = \frac{\varepsilon \mathrm{H}^2}{\sigma W_u} \tag{16}$$

is a convective dissipation timescale.

For Eq. (3b), we are interested in the conditions in which hydrostatic balance is satisfied. Hence, it will be convenient to assume that $B$ is of the same order of magnitude as the vertical pressure gradient force, yielding the following scaling:

$$B \sim \frac{\mathrm{LU}}{\mathrm{H}\tau_\epsilon}\hat{B}. \tag{17}$$

The scaling of Eq. (7) will be based on the conditions in which WTG balance is satisfied. As such, we will assume that the diabatic heating scales as:

$$Q \sim \mathrm{W}N^2\hat{Q}. \tag{18}$$

With the scales defined we write the nondimensional momentum equations as:

$$\mathrm{Re}_c \frac{D\hat{\mathbf{v}}}{D\hat{t}} = -\hat{\nabla}_h \hat{p}' - \frac{\mathrm{Re}_c}{\mathrm{Ro}}\mathbf{k} \times \hat{\mathbf{v}} + \frac{\partial^2 \hat{\mathbf{v}}}{\partial \hat{z}^2} \tag{19a}$$

$$\mathrm{Re}_c \frac{\mathrm{H}^2}{\mathrm{L}^2}\frac{D\hat{w}}{D\hat{t}} = -\frac{\partial \hat{p}'}{\partial \hat{z}} + \hat{B} + \frac{\mathrm{H}}{\mathrm{L}}\frac{\partial^2 \hat{w}}{\partial \hat{z}^2} \tag{19b}$$

$$\mathrm{Re}_c \frac{\tau_g^2}{\tau^2}\left(\frac{\partial \hat{B}}{\partial \hat{t}} + \hat{\mathbf{v}}\cdot\hat{\boldsymbol{\nabla}}_h \hat{B}\right) + \hat{w} = \hat{Q} \tag{19c}$$

where

$$\mathrm{Re}_c \equiv \frac{\tau_\epsilon}{\tau} = \frac{\varepsilon \mathrm{H} M}{M_u} \tag{20}$$

is a "convective" Reynolds number, the ratio between domain-scale acceleration and convective momentum transports, $M = \rho \mathrm{W}$ is the domain-mean mass flux,

$$\tau_g = \frac{\mathrm{L}}{c} \tag{21}$$

is the gravity wave adjustment timescale, the timescale in which gravity waves eliminate temperature anomalies from the column (Herman and Raymond 2014; Ruppert and Hohenegger 2018; Adames et al. 2019), and $c = N\mathrm{H}$ is the gravity wave phase speed.

When $\mathrm{Re}_c \ll 1$ the leading-order balance in the horizontal momentum equation is DGW balance (Fig. 2). The leading balance in the vertical momentum equation is hydrostatic balance. These two balances are written in dimensional form as:

$$\boldsymbol{\nabla}_h p' \simeq \mu_c \frac{\partial^2 \mathbf{v}}{\partial z^2} \tag{22a}$$

$$\frac{1}{\rho}\frac{\partial p'}{\partial z} \simeq B. \tag{22b}$$

Furthermore, if $\tau_g \ll \tau$ the leading-order balance in the thermodynamic equation is WTG balance:

$$wN^2 \simeq Q. \tag{22c}$$

These balances are the same as those found by Romps (2012b), except that we are representing the cloud drag in terms of a vertical diffusion.

We can show that the conditions in which the DGW approximation are valid are associated to those of widespread convection under low vertical wind shear. These conditions are associated with a large bulk Richardson number, the ratio between parcel-based convective available potential energy (CAPE) and the large-scale kinetic energy (Weisman and Klemp 1986). For the purposes of scaling, we assume that the parcel-based CAPE is proportional to $\mathrm{W}_u^2/2$ so that the bulk Richardson number can be defined as $\mathrm{Ri}_B = {\mathrm{W}_\mathrm{u}}^2/\mathrm{U}^2$. Using Eqs. (20) and (12) we find that $\mathrm{Re}_c^2 \propto \mathrm{Ri}_B^{-1}$. Thus, when $\mathrm{Re}_c$ is small $\mathrm{Ri}_B$ tends to be large.

By taking the horizontal divergence of Eq. (22a), and invoking Eq. (3c), and combining with Eq. (22b) we obtain an equation that relates $w$ and $B$:

$$\frac{\partial^3}{\partial z^3}\left(\frac{1}{\rho}\frac{\partial \rho w}{\partial z}\right) \simeq -\frac{\rho}{\mu_c}\nabla_h^2 B \tag{23}$$

where we have treated $\mu_c$ as a constant[1]. Examination of Eq. (23) reveals that the domain-mean vertical motion is not determined by $B$, but by its horizontal Laplacian. Emanuel et al. (1994) found a similar result in their strict quasi-equilibrium formulation, except the left-hand side of Eq. (23) is replaced by the tendency in $\partial_z^2 \rho w$.

Previous studies have estimated values of $\epsilon$ that range from $10^{-4}$ to $10^{-3}$ m$^{-1}$ (Romps 2010, 2014; Hannah 2017; Becker et al. 2018; Becker and Hohenegger 2021). Deep convection can have a depth of 10-15 km, hence the scale H is on the order of 4-5 km [2]. When considered together, the product $\epsilon$H has a value between 1-10. Thus, it follows that $M \ll M_u$ for $\mathrm{Re}_c \ll 1$. Furthermore, H $\ll$ L, and Ro $\geq$ 1 for Eq. (23) to be valid. In other words, $\tau \gg \tau_\epsilon$ and $\tau \lesssim \zeta_a^{-1}$ for DGW balance to hold, and $\tau \gg \tau_g$ for WTG balance to hold. We can obtain two different scenarios in which these conditions are satisfied.

### *a. Tropical Cloud Clusters*

The first case to consider is a region of active convection of $L \sim 100$ km across where updrafts occupy roughly a tenth of the domain $\sigma \sim 10^{-1}$. Several events captured during the Green Ocean Amazon (GoAmazon) field campaign near Manaus, Brazil (Fig. 3b,c) show updrafts and downdrafts that peak from 3-10 m s$^{-1}$. For the purpose of scaling, we will use a value of $\mathrm{W}_u$ of 10 m s$^{-1}$. With $H = 5$ km, Eq. (16) thus implies that $\tau_\epsilon \sim 10^4$ s, or roughly 3 hours. For long-lived tropical cloud clusters with lifetimes $\sim$ 1 day and weak near-equatorial rotation ($\zeta_a \sim 10^{-5}$s$^{-1}$), $\tau \gg \tau_\epsilon$ and Ro$\sim$ 1. We therefore find that for long-lived cloud clusters $\mathrm{Re}_c \sim 0.1$, implying that these systems are in DGW balance.

If the domain-scale winds are on the order of 1 m s$^{-1}$ it follows through mass continuity that W $\sim 10^{-1}$ m s$^{-1}$ and $\mu_c \sim 10^3$ Pa s from Eq. (2).

From Eq. (15), we find that $p' \sim$5 Pa, and from (18) we find: $B \sim 10^{-2}$ m s$^{-2}$ and $T' \sim 0.3$ K, where we have assumed an environmental temperature of $\sim$270 K. If we scale the convective available potential energy (CAPE = $\int B dz$) of the cloud cluster as $B$H we obtain a value of 100 J kg$^{-1}$. Thus, the buoyancy and CAPE are small in these clusters, consistent with both observations and with quasi-equilibrium thinking (Emanuel et al. 1994; Singh and O'Gorman 2013; Ahmed and Neelin 2018; Ahmed et al. 2020; Adames et al. 2021). Note that the CAPE we

[1]The parameter $\mu_c$ should vary in space since it depends on the the vertical mass flux of small-scale updrafts and downdrafts. Hence, Eq. (23) is likely inaccurate outside of the core region of precipitation.

[2]As shown in the following section, the vertical scale is equal to the vertical wavelength divided by $2\pi$.

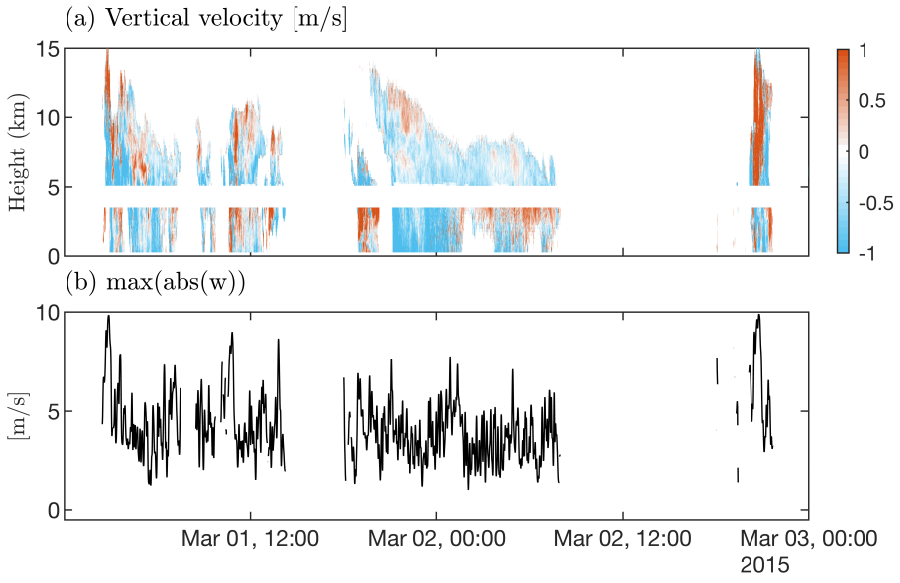


FIG. 3. (a) Vertical velocity ($w$) derived from the merged WACR-ARSCL-RWP dataset at the location of the T3 ARM site. (b) Maximum absolute value of vertical velocity for March 1st and 2nd, 2015.

have defined is an average over a scale of 100 km or so, and does not correspond to the CAPE of individual parcels within the cloud cluster.

*b. Weak large-scale acceleration near the equator*

A second case worth considering is for a domain of $L \sim 1000$ km that has active convection covering a small fraction of the domain, so that $\sigma \sim 0.01$. With $H = 5$ km, Eq. (16) now implies that $\tau_\epsilon \sim 1$ day. Thus DGW will be satisfied for timescales $\sim 10$ days, or for the near-steady cloud ensemble. Since we are near the equator the Rossby number will often be of order unity or larger, satisfying the other condition required from DGW balance. For horizontal flows on the order of 1 m s$^{-1}$ we find that W $\sim 10^{-2}$ m s$^{-1}$. This scaling is consistent with the domain sizes that are employed using WTG or DGW modeling of tropical deep convection (Wang et al. 2013; Daleu et al. 2015, 2016). In such a case $\mu_c \sim 10^2$ kg m$^{-1}$ s$^{-1}$, an order of magnitude smaller than the case for tropical cloud clusters. However, due to the larger domain size the anomalies in pressure, temperature, and buoyancy are comparable to the aforementioned case (see Eq. 15).

## 4. Dominance of the first baroclinic mode and nonlocality

Equation (23) reveals details about DGW balance that are best elucidated by examining the structure of an idealized solution. In Fig. 4 we show the circulation associated with a buoyancy given by the equation $B = B_0(\cos kx + 0.05\cos 3kx)(\sin mz - 2\sin 2mz)$, where $B_0 = 10^{-2}$ m s$^{-2}$ is an initial buoyancy anomaly, $k$ and $m$ are the zonal and vertical wavenumbers, which are related to the horizontal and vertical scales of the last section as in Adames (2022):

$$k = \frac{1}{\mathrm{L}} \qquad\qquad m = \frac{1}{\mathrm{H}}. \tag{24}$$

Note that $k$ and $m$ can also be related to the horizontal and vertical wavelengths of the system. These wavelengths can be obtained by multiplying L and H by a factor of $2\pi$. For simplicity, we have neglected variations in the y-direction. We have also assumed a Boussinesq atmosphere with rigid lids at the surface and at the tropopause. The equation was chosen to highlight how spatial variations in $B$ affects the structure of the circulation.

A salient feature of Fig. 4 is that $w$ exhibits a profile that is reminiscent of a first baroclinic mode that is slightly elevated, even though $B$ exhibits a profile that is dominated by the second baroclinic mode. This result is due to the vertical differentiation of $w$ in Eq. (23). We can interpret this result in two ways. One way is that $w$ responds more strongly to first baroclinic anomalies in $B$ than higher vertical modes. We can see this dependence more clearly after plugging in wave solutions of the form $w = w_0 \exp[i(kx + mz)]$ into Eq. (23)—and similarly for $B$—to get:

$$\frac{w_2}{w_1} = \frac{m_1^4}{m_2^4}\frac{B_2}{B_1} \tag{25}$$

where the numbered subscripts indicate the first and second baroclinic mode. By examining Eq. (25) we see that the amplitude of the second baroclinic $w$ is smaller than those

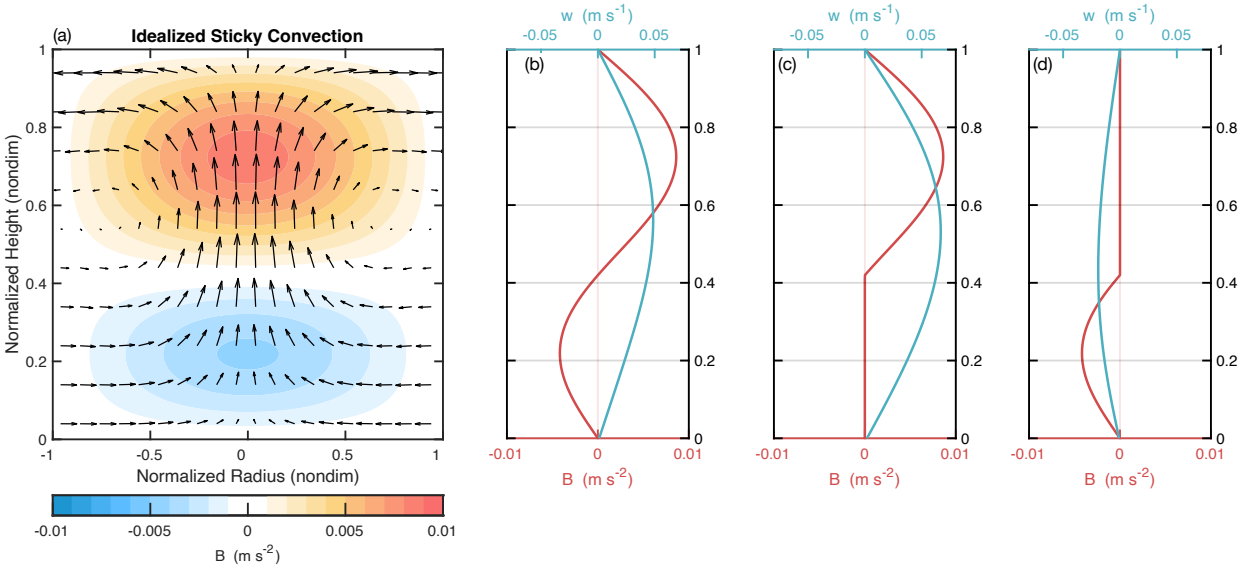


FIG. 4. (a) Circulation (arrows) associated with buoyancy field in accordance to the DGW approximation (Eq. (23)). The radius and height are normalized with respect to the system's horizontal and vertical scale (L and H, respectively). (b) Buoyancy (red) and vertical velocity (cyan) corresponding to the center of panel (a). (c) As in panel (b) but only showing the positive component of the buoyancy and the vertical velocity that is associated with it, according to

of the first baroclinic mode by a factor of 16, all else being equal.

We can also interpret the results in Fig. 4 as $w$ responding nonlocally to fluctuations in $B$, as in Kuo and Neelin (2022). To understand this better, let us consider the positive and negative contributions to $B$ in isolation, as shown in panels (c) and (d) of Fig. 4. In both panels we see that $w$ extends through the depth of the troposphere even though the contributions to $B$ do not. The profiles of $w$ and $B$ in Fig. 4b are the sum of panels c and d. Since the upper tropospheric contribution to $B$ is of larger magnitude, it follows that it dominates the distribution of $w$.

Another feature is that the ascending motion is horizontally narrower than $B$ as seen in the separation of the upward-pointing arrows and the shading in Fig. 4a. By examining Eq. (23) we see that this is a result of the horizontal Laplacian, which accentuates smaller-scale features in the distribution of $B$.

To better understand why Eq. (25) has such a strong dependence on vertical wavenumber, we use the relationship between the Brunt-Vaisala frequency ($N$) and the gravity wave speed:

$$N = cm = \frac{m}{k\tau_g}. \tag{26}$$

We further use (16) and assume that:

$$m = \frac{1}{H} = \sqrt{\frac{\rho}{\tau_\epsilon \mu_c}}. \tag{27}$$

Combining Eqs. (27), (26) and (25) with WTG balance (Eq. 22c) gives:

$$\frac{Q_2}{Q_1} = \frac{\tau_{\epsilon 2}}{\tau_{\epsilon 1}} \frac{\tau_{g1}^2}{\tau_{g2}^2} \frac{B_2}{B_1}. \tag{28}$$

Note that the vertical wave numbers are now implicit in $\tau_\epsilon$ and $\tau_g$. Under DGW balance, $\tau_g^2$ is inversely related to the horizontal Laplacian of pressure – i.e. the convergence of the pressure gradient force – that gravity waves induce on the cloud cluster. Since the length of $\tau_g$ is proportional to $m$, it follows from Eq. (25) that that gravity waves induce a convergence that is four times stronger in first barolinic motions than in second baroclinic motions. The other contribution to the vertical wavenumber dependence comes from $\tau_\epsilon$, which is four times shorter in second baroclinic motions than in first. In this case, the shorter $\tau_\epsilon$ implies that second baroclinic motions are dampened four times more than first baroclinic motions. Thus, the dominance of the first baroclinic mode implied by the form of the DGW approximation shown in Eq. (22a) is due to the combined effects of gravity wave-driven acceleration favoring the first mode, and diffusion strongly damping higher vertical modes.

## 5. Adjustment to DGW balance and Convective Quasi-equilibrium

### *a. Adjustment to DGW balance*

In order to better understand Eq. (23), it is instructive to consider how the atmosphere adjusts to this balance within an idealized setting. We will use the Boussinesq and rigid lid assumptions of the previous section, and assume that the atmosphere remains in hydrostatic balance, but will make no assumptions about DGW nor WTG balance being achieved a-priori. If we ignore the horizontal advection of temperature and momentum, we can write the vertical momentum and thermodynamic equations as:

$$\frac{\partial}{\partial t}\frac{\partial^2 w}{\partial z^2} = \nabla_h^2 B + \frac{\mu_c}{\rho}\frac{\partial^4 w}{\partial z^4} \tag{29a}$$

$$\frac{\partial B}{\partial t} = -wN^2 + Q \tag{29b}$$

By combining Eqs. (29a) and (29b), and asssuming a wave solution of the form $w = w_0 e^{i(kx+mz)}$, we obtain the equation for a forced and damped wave:

$$\frac{\partial^2 B}{\partial t^2} + \frac{1}{\tau_\epsilon}\frac{\partial B}{\partial t} + \frac{B}{\tau_g^2} = \frac{\partial Q}{\partial t} + \frac{Q}{\tau_\epsilon}. \tag{30}$$

We can simplify Eq. (30) by first considering its nondimensional form. Following the scale analysis from section 3, we obtain:

$$N_w \frac{\partial^2 \hat{B}}{\partial \hat{t}^2} + \mathrm{Re}_c \frac{\tau_g^2}{\tau_\epsilon^2}\frac{\partial \hat{B}}{\partial \hat{t}} + \hat{B} = \mathrm{Re}_c \frac{\partial \hat{Q}}{\partial \hat{t}} + \hat{Q}. \tag{31}$$

The number $N_w = \tau_g^2/\tau^2$ describes the gravity wave-driven adjustment towards WTG balance (Ruppert and Hohenegger 2018; Adames 2022). For first baroclinic systems of scales of 100 km, $\tau_g$ is on the order of 30 minutes (Fig. 5). For this and comparable horizontal scales, $\tau_g$ is much shorter than $\tau_\epsilon$. As a result, for systems in which $\mathrm{Re}_c \ll 1$ it follows that $N_w$ must be even smaller, on the order of $10^{-3}$. Furthermore, as stated above, $\tau_\varepsilon$ is on the order of 2-3 hours, so that $\tau_\varepsilon^{-2}\tau_g^2 \ll 1$. Since we are only considering the case when $\mathrm{Re}_c \ll 1$, it follows that the first two terms on the left-hand side of Eq. (31) are at least two orders of magnitude smaller than the largest term, while the heating tendency is roughly an order of magnitude smaller.

If we retain the largest and second-largest terms in Eq. (30) we obtain the following

$$\frac{\partial Q}{\partial t} = \frac{B}{\tau_g^2} - \frac{Q}{\tau_\epsilon} \tag{32}$$

From Eq. (32) we see that $B$ is a source for $Q$. How much $B$ increases $Q$ depends on $\tau_g^2$, indicating that the acceleration is driven by the damped gravity waves. The second term is the damping of the convective region via diffusion by the turbulent elements within it. From this term we see that the convective adjustment timescale in this framework is $\tau_\epsilon$. For the first baroclinic mode, this timescale is close to the convective adjustment timescale estimated from Ahmed et al. (2020) as well as commonly-used values in convective parameterization schemes (e.g., Zhang and McFarlane 1995a; Gregory et al. 2000).

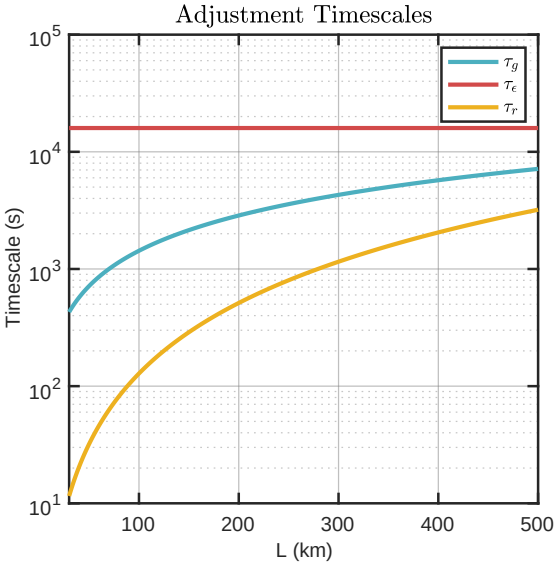


FIG. 5. The timescales $\tau_g$ (blue), $\tau_\epsilon$ (red), and $\tau_r$ (yellow) as a function of the horizontal scale L. Only the first baroclinic vertical mode is shown, with $c = 50$ m s$^{-1}$.

More insights onto Eq. (32) can be obtained by examining the response of convection to a constant $B$ anomaly that is turned on at $t = 0$. In this case, the solution to Eq. (32) takes the form:

$$Q(t) = \frac{\tau_\epsilon}{\tau_g^2} B\left(1 - e^{-\frac{t}{\tau_\epsilon}}\right). \tag{33}$$

As shown in Fig. 6 heating quickly responds to the $B$ anomaly. For the case in which $\tau_\epsilon = 2$ hours, equilibrium is approximately achieved in about four hours, so that the leading-order balance is joint DGW-WTG balance:

$$\frac{B}{\tau_g^2} \simeq \frac{Q}{\tau_\epsilon}. \tag{34}$$

It is worth pointing out that Eq. (34) is identical to the strong friction limit of vertical velocities found by Hernandez-Duenas et al. (2019) after applying the WTG approximation.

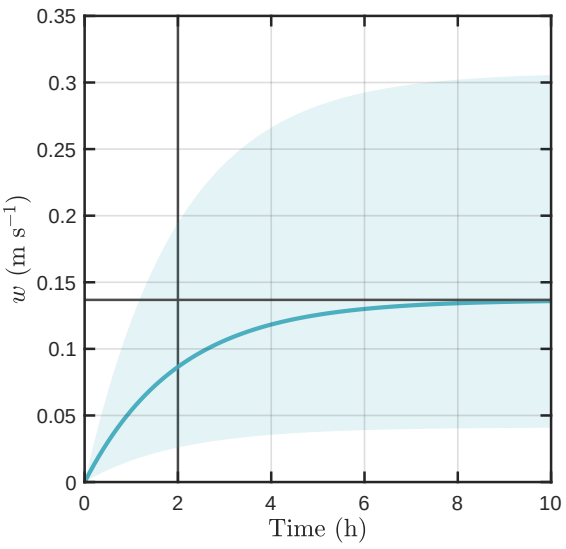


FIG. 6. Response to heating ($Q$) to a $B$ anomaly of $10^{-2}$ m s$^{-2}$ that is turned on at $t = 0$, following Eq. (33). The cyan line shows the case when $\tau_\epsilon = 2$ hours, while the shaded area denotes the range of value that $Q$ has if we vary $\tau_\epsilon$ from 30 minutes to 5 hours. A constant value of $\tau_g$ of 30 minutes is used. The vertical solid gray line depicts the value of $\tau_\epsilon$, which behaves as the convective adjustment timescale under WTG-DGW balance. The horizontal gray line denotes the equilibrium value of $Q$.

### b. *Convective Quasi-Equilibrium*

The DGW approximation yields a form of convective quasi-equilibrium that is worth elaborating upon. We can show this by integrating Eq. (34) vertically from the cloud base to the level of neutral buoyancy. Additionally, we will also define a "convective response timescale" as $\tau_r = \tau_g^2/\tau_\epsilon$, which yields the following:

$$\langle Q \rangle \simeq \frac{\rho \mathrm{CAPE}}{\tau_r} \tag{35}$$

where the angle brackets denote a mass-weighted vertical integral ($\langle Q \rangle = \int_0^{z_t} Q \rho dz$, where $z_t$ is the tropopause height).

Equation (35) is reminiscent of the CAPE-based parameterizations of convection often employed in GCMs (Zhang and McFarlane 1995b; Gregory et al. 2000). These treatments define $\tau_r$ as the convective adjustment timescale since it is also the timescale in which CAPE is removed in these parameterizations. However, the convective adjustment timescale is $\tau_\epsilon$, not $\tau_r$ (Eq. (32)). According to Eq. (35), $\tau_r$ describes the sensitivity of convection to fluctuations in CAPE. Furthermore, $\tau_r$ is not a constant, but is dependent on the horizontal and vertical wavenumbers. In Fig. 5 we see that $\tau_r$ ranges from 10 s for spatial scales of 50 km, to roughly one hour at scales closer to 500 km for a precipitating region with a first baroclinic profile of vertical velocity. Thus, preciptation is more sensitive to small-scale fluctuations in CAPE than to large-scale fluctuations.

## 6. DGW-WTG balance, Entraining Convective Quasi-equilibrium and the Precipitation-Buoyancy Relationship

We will now use the DGW-WTG approximations to understand how precipitation is related to measures of buoyancy. We will also make connections to the entraining plume-based tropical precipitation-buoyancy framework (Ahmed and Neelin 2018; Schiro et al. 2018). We begin by noting that the expression in Eq. (34) can be written in terms of precipitation by multiplying it by $C_p T_e/g$ and performing a mass-weighted vertical integral:

$$L_v P = \frac{1}{\tau_r} C_p \langle T' \rangle - \langle Q_r \rangle - F_s \tag{36}$$

where $\langle Q_r \rangle$ is the column-integrated radiative heating rate and $F_s$ is the surface sensible heat flux. Only non-negative values of $P$ are allowed in Eq. (36).

From Eq. (36) we infer that precipitation will occur only if $T'$ exceeds a threshold value. This value is given by a column-averaged value of $T'$ of $\approx -0.007$ K if we assume that $\langle Q_r \rangle + F_s = -100$ W m$^{-2}$. Larger $T'$ values are associated with a linear increase in precipitation. This pickup curve, shown in Fig. 7, is reminiscent the precipitation-buoyancy relation discussed by Ahmed et al. (2020). The scaling arguments used in the previous section suggest that $\tau_r$ is on the order of 10 minutes. With this timescale, a tropospherically-averaged temperature anomaly of 0.1 K yields a precipitation rate of nearly 2000 W m$^{-2}$ or 60 mm day$^{-1}$ (Fig. 7). Thus, only small temperature anomalies are needed to produce large rainfall rates.

From examination of Eq. (36) one would be tempted to assume that precipitation is only sensitive to temperature under DGW-WTG balance. However, it is well known that the boundary layer moist static energy (MSE) and free tropospheric moisture play an important role in the onset and evolution of convection (Lucas et al. 1994; Donner and Phillips 2003; Ahmed and Neelin 2018). We will now show how these variables impact the convective quasi-equilibrium discussed in Section 5 and may explain the buoyancy field of the DGW approximation.

### a. *Entraining Convective Quasi-Equilibrium*

Consider a cloud cluster that is in WTG and DGW balances, as in Fig. 2. Since $T'$ is small, we can follow Arakawa and Schubert (1974); Moorthi and Suarez (1992), and Adames et al. (2021) to express it in terms of moist

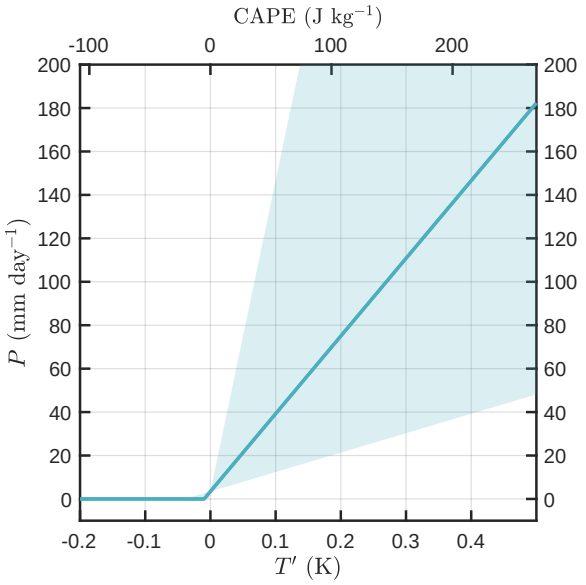


FIG. 7. Precipitation as a function of the mean tropospheric temperature anomaly following Eq. (36). A value of $\langle Q_r \rangle + F_s$ of −100 W m$^{-2}$ is used, and $\tau_r$ = 15 minutes. The shaded region encompasses the region where the curve would be at for $\tau_r$ values between 3.75 and 60 minutes. The corresponding CAPE value is shown as the top x-axis.

static energy (MSE):

$$C_p T' \simeq \frac{1}{\kappa}\left(h^* - h_e^*\right); \qquad \kappa = 1 + \frac{L_v^2 q_e^*}{C_p R_v T_e^2} \tag{37}$$

where $R_v$ is the gas constant of water vapor, $q$ is the specific humidity, $h = C_p T + gz + L_v q$ is the MSE, and asterisks indicate the saturation value. The subscript $e$ refers to the environment outside the cloud cluster, as in the previous sections.

Since the cluster experiences dilution from both dynamic and turbulent entrainment (De Rooy et al. 2013), it follows that $h^*$ will be less than what is expected from undilute moist adiabatic ascent. To account for this dilution, we will follow Wolding et al. (2022) and decompose $h^*$ into undilute and dilution components:

$$h^* = h_U^* - h_D^* \tag{38}$$

where $h_U$ is equal to the boundary layer MSE, as in Emanuel et al. (1994). The dilution of MSE can be calculated by employing an entraining plume model, as shown in Appendix B. With these definitions we may define the undilute temperature anomaly and the temperature reduction from dilution as:

$$C_p T_U' \simeq \frac{1}{\kappa}\left(h_U^* - h_e^*\right) \tag{39a}$$

$$C_p T_D' \simeq \frac{1}{\kappa}\left(h_U^* - h^*\right). \tag{39b}$$

In Appendix B we show that two processes contribute to $h_D$. First, the cluster as a whole approximately behaves like an entraining plume, where the cluster-scale entrainment comes from horizontal MSE advection from the gravity wave-driven inflow. Second, since the cluster is unsaturated, the cloudy updrafts within it still experience dilution from subdomain-scale entrainment. In other words, the cluster experiences dilution from entrainment at the cluster and cloud scale. With these definitions, we use Eq. (39) to write Eq. (36) as:

$$L_v P \simeq \frac{C_p\left(\langle T_U' \rangle - \langle T_D' \rangle\right)}{\tau_r} - \langle Q_r \rangle - F_s. \tag{40}$$

Figure 8 shows the distribution of $P$ for different values of $T_U'$ and $T_D'$, arranged in a way that is similar the results of Ahmed and Neelin (2021) and Wolding et al. (2022). For small $T_D'$ and large $T_U'$ (top-right corner of Fig. 8) the cloud cluster would exhibit CAPE values on the order of > 1000 J kg$^{-1}$, values that we expect to see in thunderstorms using parcel theory. However, the rainfall rates associated to this scenario are very large, and may correspond only to the most extreme precipitation rates in the tropics. More realistic precipitation rates align closer to the $T' = 0$ line, which also corresponds to radiative-convective equilibrium. This line corresponds to undilute CAPE (CAPE$_U$) values on the order of 1000 J kg$^{-1}$ and a dilution of CAPE (CAPE$_D$) that is of comparable magnitude. The two components nearly cancel, so that the actual CAPE of the convective region shown in Fig. 7 is on the order of 100 J kg$^{-1}$. That most precipitation rates occur near the $T' = 0$ (CAPE = 0) line implies that, at scales of ∼ 100 km tropical deep convection is in an entraining convective quasi-equilibrium (Ahmed et al. 2020, 2021; Duan et al. 2024). It also indicates that cloud clusters in DGW-WTG balance are small excursions from the zero buoyancy approximation used by Singh and O'Gorman (2013).

### b. *DGW-WTG balance and the precipitation-buoyancy relation*

The precipitation in the undilute-dilute phase space from Fig. 8 is interpreted as the two-dimensional extension of the precipitation-buoyancy relationship of Ahmed and Neelin (2018, 2021). The semi-empirical precipitation-buoyancy relation presented in Eq. (8) of Ahmed et al. (2020) is:

$$P = a(B_L - B_c)\mathcal{H}(B_L - B_c) \tag{41}$$

where $B_L$ is the plume buoyancy averaged over the lower-free troposphere, $B_c$ is a critical buoyancy value, $\mathcal{H}$ is the Heaviside step function, and $a$ is a constant. It is important to note that the definition of buoyancy that is

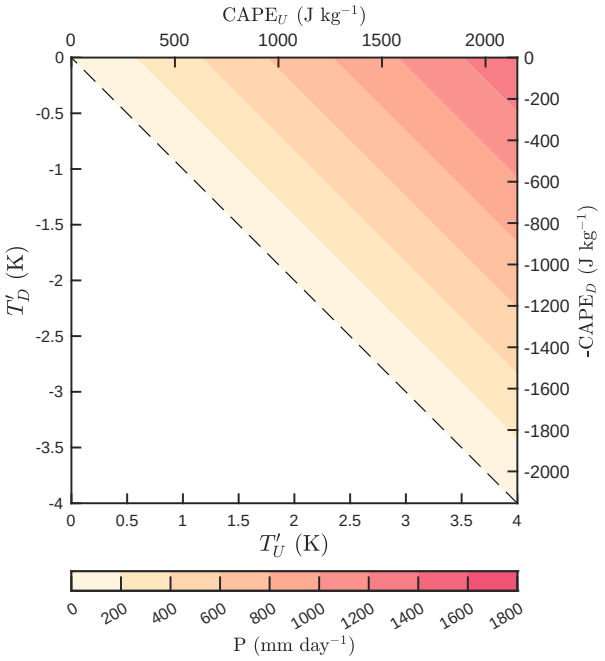


FIG. 8. Precipitation as a function of undilute temperature anomaly ($T'_U$) and saturation deficit ($q^+$) following Eq. (40). The dashed horizontal line corresponds to $T' = 0$, the line in which the buoyancy of the region is zero. The corresponding undilute CAPE (CAPE$_U$) and dilution of CAPE (CAPE$_D$) are shown as the x-axis on the top and y-axis on the right, respectively.

usually employed in Eq. (41) invokes the MSE of the plume (or equivalent potential temperature), rather than the saturation MSE, i.e.:

$$B = g\frac{h - h_e^*}{\kappa C_p T_e}. \tag{42}$$

While this relation was originally obtained semi-empirically, we can derive it from the basic equations when we assume that the convection is in WTG-DGW balance. For the sake of illustration, let us assume that $B_L$ is approximately equal to its tropospheric-mean value, i.e. $B_L \sim \langle B\rangle \rho^{-1} z_t^{-1} \sim z_t^{-1}$CAPE, where $z_t = 15$ km. This is a reasonable approximation if we only take into account first baroclinic vertical motions. Furthermore, since cloud clusters have an MSE that can be well below the saturation value, we must separate it into its saturation and decifit ($h^+$) components in order to relate Eq. (41) to Eq. (36):

$$h = h^* - h^+ \tag{43}$$

where $h^+$ is the saturation deficit of the cloud cluster's MSE.

To facilitate making the connection between Eq. (41) and Eq. (36), we are taking $T_e = 260$ K, $\kappa = 2$, and $\rho = 0.7$ to be constants with values roughly equal to their vertical averages. After making these assumptions and combining Eqs. (34) and (36) we arrive at the following definitions for the constants in Eq. (41):

$$a \sim \frac{C_p T_e \rho z_t}{L_v \tau_r g}; \qquad B_c \sim -\frac{\langle h^+\rangle}{L_v \kappa a \tau_r}. \tag{44}$$

Using these values and $\tau_r = 15$ m, we find that $a = 0.12$. From Eq. (B9) we see that $h^+$ decays exponentially with height, and only depends on the surface $h^+$ and $\varepsilon$. In Fig. B1 we that the surface $h^+$ tends to have a value between $0.5{-}2\times10^4$ J kg$^{-1}$. By assuming a constant value of surface $h^+$ of $10^4$ J kg$^{-1}$, and following the discussion in Appendix B we find that $B_c \approx -0.017$ m s$^{-2}$. We have dropped the contributions of $\langle Q_r\rangle + F_s$ to $B_c$ since it is much smaller than the contribution from $h^+$.

In Fig. 9 we compare the theoretically-derived values of Eq. (41) with precipitation and buoyancy from ERA5, calculated as in Vargas Martes et al. (2023). Further details are provided in Appendix C. We see that using realistic values in the definitions of $a$ and $B_c$ yields a pickup curve from DGW-WTG balance that agrees well with the mean value of the distribution of points from ERA5 data. Furthermore, the precipitation picking up at negative $B_L$ values in Fig. 9 is explained as resulting from $B_L$ being defined in terms of $h$ rather than $h^*$. The missing contribution from $h^+$ is accounted for in $B_c$. If $B_L$ were defined using $h^*$ instead, the pickup would occur at near-zero buoyancy. The slope of the curve is largely determined by $\tau_r$, which can have a variety of realistic values. The green lines in Fig. 9 show how the curve would look like if $\tau_r$ were increased or decreased by a factor of four. While varying $\tau_r$ can weaken the fit between observations and theory, the pickup curve is steep even when $\tau_r$ is substantially varied since it is still on the order of minutes.

The only significant disagreement between the reanalysis-based precipitation-buoyancy relation and Eq. (42) is the near exponential pickup of the precipitation for $B_L$ values that are slightly smaller than $B_c$. Some of this pickup may be due to variations in $h^+$, or from stochastic variations in $B_c$ occurring around the DGW-WTG balance, similar to what Ahmed et al. (2020) found for the precipitation-moisture relation.

## 7. Summary and Conclusions

It is well known that deep convection can dissipate momentum in the free troposphere (Houze Jr 1973; Chang 1977; Mapes and Wu 2001; Lin et al. 2008). Many studies have invoked its use as a form of friction in the momentum budget of large-scale tropical circulations (Gill 1980; Lin et al. 2005; Majda and Stechmann 2008; Kim and Zhang 2021). Furthermore, it became the physical basis behind the DGW approximation, which has been used to represent large-scale ascent in regional simulations of deep convection (Kuang 2008; Wang et al. 2013; Herman and Raymond

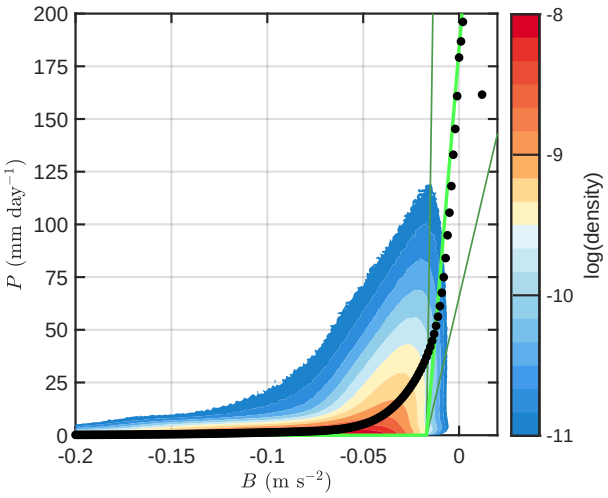


FIG. 9. Base 10 logarithm of the normalized distribution of $P$ vs $B_L$ for ERA5 output over the 15°N–15°S latitude belt. The values of $P$ are binned every mm day$^{-1}$ while $B_L$ is binned every 0.0015 m s$^{-2}$. The circles show the mean value of the distribution. The light green line corresponds to the curve obtained from Eq. (41) and (44) using the $\tau_r$ value of 15 m used in Fig. 7. Thin dark green lines are as in the light green line but for $\tau_r$ values of 3.75 and 60 minutes.

2014; Daleu et al. 2016). Motivated by these studies, our study examines the possibility that mesoscale regions of deep convection may be in DGW balance, i.e., their momentum balance is characterized by a balance between the pressure gradient force and dissipation driven by cumulus momentum transport. These transports are represented as a vertical momentum diffusion.

Below are the answer to the questions outlined in section 1:

*a. When is the DGW approximation valid?*

Scale analysis of the basic equations in Cartesian coordinates suggests that DGW balance can occur when a non-dimensional parameter we refer to as the convective Reynolds number ($\mathrm{Re}_c$, Eq. 20) is much smaller than unity. This number is small when the timescale of the convective region is longer than the timescale in which small-scale turbulence dissipates momentum. We found that this condition could be valid for tropical cloud clusters with horizontal scales on the order of 100 km and timescales close to a day. The number $\mathrm{Re}_c$ can also be small near the equator at scales of 1000 km when acceleration is weak. This is the condition that is often assumed when modeling tropical deep convection in a limited domain (Wang et al. 2013; Daleu et al. 2015).

*b. Can the DGW approximation explain the preponderance of the first baroclinic vertical velocity profile in the tropics?*

Under the DGW approximation, momentum diffusion by small-scale elements in convection as well as the forced gravity wave response to convection cause the first baroclinic mode to be 16 times stronger than the second baroclinic mode, assuming that the buoyancy anomalies of the two modes are of equal amplitude. This relationship between ascent and buoyancy makes the vertical velocity response to buoyancy nonlocal (Fig. 4). Ascent can occur in regions of negative buoyancy so long as a stronger positive buoyancy exists at another tropospheric layer.

Given that vertical velocities in the deep tropics largely reflect those of convection, it follows that the DGW approximation can explain the preponderance of the first baroclinic mode in the tropics. It should be noted that the second baroclinic mode in observations is smaller than the second mode by a factor of ~ 4 (Back et al. 2017; Inoue et al. 2020). If we account for fluctuations in temperature being stronger in the higher baroclinic modes, then this difference can be reconciled.

*c. Can the DGW approximation explain the linear relationship between buoyancy and rainfall?*

When the DGW approximation is combined with the weak temperature gradient (WTG) approximation we find that the cloud clusters are in convective quasi-equilibrium (Arakawa and Schubert 1974; Yano and Plant 2012). Unlike conventional forms of quasi-equilibrium the convective adjustment timescale — equal to the dissipation timescale ($\tau_\epsilon$) under the DGW approximation — does not describe the the sensitivity of precipitation to CAPE. Rather, this sensitivity is described by the ratio of the square of the gravity wave adjustment timescale and the dissipation timescale ($\tau_r = \tau_g^2/\tau_\epsilon$). At the scale of cloud clusters $\tau_r$ is much smaller than $\tau_\epsilon$, rendering rainfall highly sensitive to CAPE fluctuations. The DGW approximation also reveals that this sensitivity is tightly related to gravity waves, as implied by $\tau_g$.

Considering the cloud cluster as an entraining plume yields the precipitation-buoyancy of Ahmed and Neelin (2018). We can explain the sharp pickup of rainfall after a critical buoyancy is reached as a result of the smallness of $\tau_r$. The critical buoyancy itself arises from the fact that the $P - B$ relation uses MSE (or theta-e) of the cluster, rather than its saturation value. The critical buoyancy accounts for this difference. When this difference is accounted for, we see that large rainfall rates result from small positive buoyancy anomalies (Fig. 8), a form of entraining convective quasi-equilibrium (Ahmed et al. 2020; Duan et al. 2024). We can also interpret the precipitation-buoyancy relation as the result of small excursions from the zero buoyancy approximation (Singh and O'Gorman 2013;

Singh and Neogi 2022). Since varying amounts of stability and tropospheric moisture can lead to the same buoyancy in the entraining plume framework, the results presented here may also be related to the moisture quasi-equilibrium discussed by Raymond et al. (2015) and Sessions et al. (2019), although we do not examine how moisture and stability are related to the vertical velocity profile.

*d. Additional implications*

Although we have emphasized how the DGW approximation can help us answer the three questions outlined in section 1, the results also depend on the system being in WTG balance. When this balance is satisfied, the nondimensional number $N_w$ from (31) is much smaller than unity, and in the cloud clusters examined here we found that this number is on the order of $10^{-3}$. Using the definition of $N_w$ we can redefine $\tau_r$ as:

$$\tau_r = \tau \frac{N_w}{\mathrm{Re}_c}. \tag{45}$$

From this equation we see that the rapid increase in rainfall after a critical buoyancy is reached is largely due to the smallness of $N_w$.

The implication of this scaling is that the fast adjustment towards WTG balance rapidly eliminates buoyancy in the tropics, and hence regions of heavy rainfall are associated with small buoyancy anomalies. It follows that convective quasi-equilibrium and the zero-buoyancy approximation can be interpreted as consequences of WTG balance being enforced since WTG balance does not allow for large deviations from this balance. A similar argument can be made for the preponderance of the first baroclinic mode by expressing Eq. (28) in terms of $N_w$. First baroclinic gravity waves are much faster than higher order gravity waves, hence the buoyancy anomalies of the first mode are quickly damped, leading to profiles that appear first baroclinic even when the buoyancy anomalies exhibit a largely second baroclinic profile (Fig. 4).

The results from Eq. (28) and Fig. 4 indicate that deep inflow profiles are robust to the vertical structure of the buoyancy anomaly — in particular, the negative buoyancy in the lower troposphere. This result suggests that deep inflow would occur within cloud clusters in DGW balance with or without well-established cold pools, so long as a positive buoyancy anomaly exists at higher elevation. Therefore, given that the deep $w$ profile suggests entrainment is occurring through a deep lower tropospheric layer, a moist lower free troposphere could sustain a region of convection even in the presence of negative buoyancy perturbations in the boundary layer. This interpretation would also apply to organized deep convective systems occurring at night in tropical continental regions when a pronounced layer of convective inhibition (CIN) is present (Schiro et al. 2016). The above is consistent with observational evidence that MCS occurrence and intensity are highly sensitive to lower free tropospheric moisture (Schiro and Neelin 2019b; Schiro et al. 2020).

Lastly, the results presented here could shed some light onto convective self-aggregation (Held et al. 1993; Bretherton et al. 2005; Wing and Emanuel 2014). If we consider a region of aggregated convection as a cluster that obeys DGW-WTG balance, it follows that its virtual temperature must be slightly higher than the surrounding environment. This is in agreement with Yang (2019), who emphasized the importance of generation of available potential energy in aggregated convection. Furthermore, the framework is also consistent with the view of aggregated convection being a moist patch surrounded by a drier environment (see reviews by Wing et al. 2018 and Muller et al. 2022). If the aggregated convection behaves like an entraining plume, the high humidity of the aggregate relative to the surrounding environment should be sufficient to maintain the buoyancy of convection, as discussed above. Thus, the two views of convective aggregation are reconcilable under the DGW-WTG approximation, indicating that applying this framework to convective self-aggregation could be viable direction for future research.

*e. Caveats*

While the use of DGW-WTG balance to understand regions of tropical deep convection yields some promising results, it still has a few limitations. First, the findings presented here depend on a large constant eddy exchange coefficient $\mu_c$ in regions of precipitation. Mapes and Wu (2001) showed that friction can be treated as a function of the precipitation rate. While their study focuses on a larger domain that contains cloud cluters, disorganized convection and cloud-free environment, it is nonetheless likely that $\mu_c$ is a function of the strength of the convection. More detailed expressions of $\mu_c$ will not change the existence of DGW balance, but it could change the precipitation-buoyancy relation discussed in Section 6. Since we do not know much about how $\mu_c$ changes with cloud organization and morphology, it is reasonable to treat it as a constant as a first step to understand motions under the DGW approximation even though it is also a limitation of this study.

Second, the results of this study were obtained by making numerous assumptions, approximations and idealizations. This makes obtaining tractable results easier, but makes the application to individual systems more limited. For instance, the results presented here hinge on having a value of $\mathrm{Re}_c$ that is much smaller than unity, which is also tied to convection occurring in regions of low shear. It is not clear how often a small $\mathrm{Re}_c$ is seen in regions of active convection. Many MCSs exhibit strong vertical wind shear (Houze 2004), which limits the application of this

framework on them. More work is needed to better understand the applicability of the DGW-WTG approximation in tropical convection.

### *f. Concluding remarks*

The results of this study show the importance of gravity waves in tropical convection. They play central roles in determining the profile of vertical velocity and in the sensitivity of rainfall to buoyancy anomalies. Thus, our results support viewing cloud cluster as a coupling between convection and gravity waves, a view that can be traced back to the work of Bretherton and Smolarkiewicz (1989), Nicholls et al. (1991), and Mapes (1993). The characteristics and strength of this coupling are ultimately dictated by the enforcement of WTG balance, highlighting more important consequences of this approximations. While DGW-WTG balance shows promise in explaining several features of tropical convection, the ideas presented here require further testing. As discussed above, examining it within the context of MCSs and convective self-aggregation seem like worthwhile directions for future research.

*Acknowledgments.* This work was supported by the National Science Foundation grant numbers AGS-2225954 (KAS), AGS-2225955 (AFAC), AGS-2225956 (FA) and AGS-2225957 (BOW) AFAC thanks Larissa Back for conversations that helped improve the contents of the manuscript.

*Data availability statement.* Ground-based observations from the GoAmazon 2014/5 field campaign can be accessed and downloaded via the DOE ARM Data Discovery portal at `https://www.arm.gov/research/campaigns/amf2014goamazon` with a free ARM user account. For more details, the Merged RWP-WACR-ARSCL Cloud Mask and Cloud Type data product is available from Feng and Giangrande (2018).

## APPENDIX A

### On the diffusive properties of subdomain-scale motions

We can understand how convection causes damping of the large-scale flow by following Romps (2014) and considering a simplified pair of equations where the only influence on the large-scale flow is cumulus momentum transport, and the only influence on the convection's horizontal winds is an effective entrainment:

$$\frac{\partial \mathbf{v}}{\partial t} = \frac{1}{\rho}\frac{\partial}{\partial z}\left[M_u(\mathbf{v}-\mathbf{v}_u)\right] \tag{A1}$$

$$\frac{\partial \mathbf{v}_u}{\partial z} = \varepsilon(\mathbf{v}-\mathbf{v}_u). \tag{A2}$$

Let us consider the case in which both fields exhibit wave solutions of the form:

$$v = v_0 \exp(imz - i\varpi t). \tag{A3}$$

By assuming that $M_u$ and $\varepsilon$ are constants we obtain the following dispersion relation:

$$\varpi = -\frac{M_u m^2}{\rho}\left(\frac{m+i\varepsilon}{m^2+\varepsilon^2}\right). \tag{A4}$$

When we consider the case when $\varepsilon \gg m$, the dispersion relation simplifies to

$$\varpi \simeq -\frac{iM_u m^2}{\rho\varepsilon} \tag{A5}$$

Equation (A5) implies that the convective momentum transport acts as a diffusion of momentum. It can be shown that Eq. (A5) can be obtained by assuming a wave solution to the following equation:

$$\frac{\partial \mathbf{v}}{\partial t} \simeq \frac{\mu_c}{\rho}\frac{\partial^2 \mathbf{v}}{\partial z^2}. \tag{A6}$$

However, we note that this approximation implies that the treatment of convective momentum as a diffusive process may be inaccurate for larger vertical wavenumbers.

## APPENDIX B

### MSE budget of cloud cluster

Within the cloud cluster we have updrafts and regions of downward motions (downdrafts and clear-air descent), denoted by the subscripts $u$ and $d$, respectively. The mean mass flux of the cluster is the sum of the upward and downward mass fluxes

$$M = M_u + M_d. \tag{B1}$$

Since the DGW approximation is valid only when $\mathrm{Re}_c \ll 1$ (Eq. 20), it follows that $M_u$ and $M_d$ must nearly cancel out, so that $M \ll M_u$. As in Singh et al. (2019) and Romps (2021), we write the mass continuity budgets of the ascending and descending regions as:

$$\frac{\partial M_u}{\partial z} = M_u(\varepsilon - \delta) \tag{B2a}$$

$$\frac{\partial M_d}{\partial z} = -M_u(\varepsilon - \delta) + C_g \tag{B2b}$$

where $\varepsilon$ and $\delta$ are the fractional entrainment and detrainment rates, respectively, and $C_g$ is the large-scale mass convergence. The subscript $g$ is used to denote that this convergence is driven by the gravity wave response to the

convection in the cluster. This contribution is responsible for the domain-mean mass flux since adding Eqs. (B2a) and (B2a) yields $\partial_z M = C_g$.

Supposing that descending air occupies most of the area of the cloud cluster, it follows that $h \simeq h_d$. Furthermore, gravity waves will largely homogenize temperatures within the cluster, so that $h^* \simeq h_u^*$. If we additionally assume that the updrafts behave as an entraining plume, we write the respective MSE budgets of the ascending and descending regions as

$$\frac{\partial h^*}{\partial z} = -\varepsilon(h^* - h) \tag{B3a}$$

$$\rho\frac{\partial h}{\partial t} + (h - h_e)\frac{\partial M}{\partial z}\mathcal{H}(C_g) + M_d\frac{\partial h}{\partial z} = M_u\delta(h_u^* - h) \tag{B3b}$$

where $\mathcal{H}$ is the Heaviside step function. Equation (B3a) is the conventional MSE budget for a steady plume. Equation (B3b), however, warrants further discussion. From left to right, the processes shown in Eq. (B3b) are the MSE tendency, horizontal MSE advection by the large-scale convergence, vertical MSE advection by descending motions, and detrainment from cloudy updrafts. These are the same equations as in Singh et al. (2019). For simplicity, we have not included the turbulent flux of MSE in Eq. (B3b) since we are largely considering motions above the boundary layer. We are also excluding the contributions from radiative heating and ice microphysics to the MSE budget. We do this to be consistent with previous work, even though these contributions may be non-negligible.

It will be insightful to add $M_u\partial_z h$ to both sides of Eq. (B3b). By invoking Eq. (B3a), using the multiplication rule, and assuming that $\varepsilon \simeq \delta$ (Romps 2014, 2021) we arrive at the following budget for the lower troposphere:

$$\rho\frac{\partial h}{\partial t} + \frac{\partial hM}{\partial z} - h_e\frac{\partial M}{\partial z} + M_u\frac{\partial h^+}{\partial z} = 0 \tag{B4}$$

Examination of the terms in Eq. (B5) reveals that the second and third terms are much larger than the rest (not shown). Hence the MSE budget of the cloud cluster is approximately related to the MSE of the surrounding environment via the following equation

$$\frac{\partial hM}{\partial z} \simeq h_e\frac{\partial M}{\partial z}. \tag{B5}$$

In the upper troposphere, horizontal MSE advection does not impact the cloud cluster, and the resulting MSE budget is written as:

$$\rho\frac{Dh}{Dt} = -M_u\frac{\partial h^+}{\partial z} \tag{B6}$$

A close look of the term on the rhs of Eq. (B6) indicates that it is too small to substantially change $h$ as it rises within the cloud cluster. Thus, we can assume that the MSE of the cloud cluster will exhibit a near-constant profile in the upper troposphere.

Following these results we can vertically integrate the MSE budget to obtain

$$h(z) \simeq \begin{cases} \dfrac{1}{M(z)}\displaystyle\int_{z_b}^{z}\frac{\partial M}{\partial z'}h_e dz' & z \le z_m \\ h(z_m) & z > z_m \end{cases} \tag{B7}$$

where $z_m$ is the height in which the mass convergence is zero. Equation (B7) is identical to Eq. (1) in Ahmed and Neelin (2018), implying that the cloud cluster approximately behaves like a plume that entrains environmental air through its mass convergence. It is worth noting that, under DGW-WTG balance, the entrainment implied in Eq. (B7) comes from the horizontal MSE advection that arises from gravity wave-driven inflow.

We now will seek to obtain an explicit expression for $h^+$. Since $h$ is nearly constant in the upper troposphere, it follows that $\partial_z h \simeq 0$. In the lower troposphere $\partial_z h$ is nonzero, but it can be shown to be smaller than $\epsilon h^+$. Thus we can manipulate Eq. (B6) to obtain the following equation for $h^+$:

$$\frac{\partial h^+}{\partial z} \simeq -\varepsilon h^+ \tag{B8}$$

which can be integrated vertically to obtain the following solution:

$$h^+ = h_0^+ e^{-\varepsilon z} \tag{B9}$$

where $h_0^+$ is the near surface value of $h^+$. In Fig. B1 we see that $h_0^+$ exhibits a value between 1 and $1.5\times10^4$ J kg$^{-1}$ in the TOGA-COARE and DYNAMO data. In contrast, there is more variation in $h_0^+$ in GO-Amazon observations, with a mode centered near 7.5 $\times10^3$ J kg$^{-1}$. This distinct distribution in GO-Amazon may reflect differences in boundary layer dynamics between land and ocean, or may be a result of the size of the sounding domain. Nonetheless, most $h_0^+$ values are centered between 0.5 and 2 $\times10^4$ J kg$^{-1}$. The low variability of $h_0^+$ may be a reflection of boundary layer quasi-equilibrium maintaining the $h$ and $h^*$ nearly fixed (Raymond 1994; de Szoeke 2018). The value of $10^4$ J kg$^{-1}$ can be obtained from $h_0^+ \simeq L_v q_{e0}^*(1 - \mathrm{RH}_e)$ when $q_{e0}^* \approx 0.02$ and when $\mathrm{RH}_e \approx 0.8$, typical values of the boundary layer in tropical precipitating regions.

In Fig. B2 we show example profiles of $h, h^*, h_e$ and $h_e^*$. While the MSE of the cloud cluster and the environment are the same near the surface, $h$ and $h^*$ decrease more slowly in the lower troposphere than $h_e$ and $h_e^*$, allowing the cloud cluster to exhibit greater buoyancy than the environment. The temperature anomalies of this profile are on the order of 1 K, much larger than what would be typical under DGW-WTG balance. This is because the sounding was built to exaggerate the difference between the MSE of the cloud cluster and the environment. In reality, the difference between the two will be smaller than what is shown in Fig. B2.

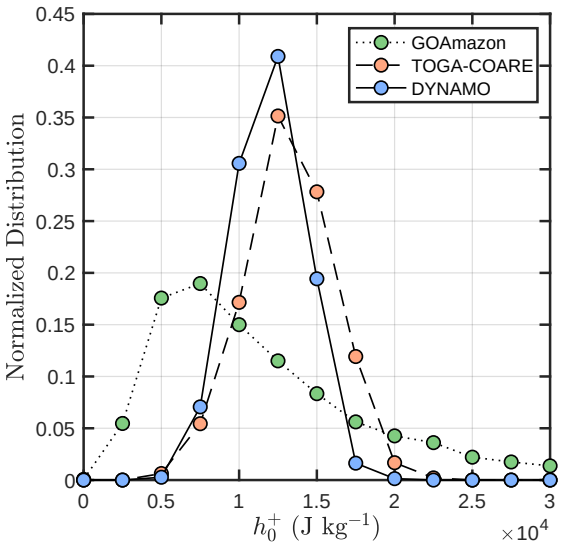


FIG. B1. Normalized distribution of 1000 hPa $h^+$ obtained from sounding data from (a) GO-Amazon, (b) TOGA-COARE, and (c) DYNAMO northern sounding array. The data is binned at intervals of 2.5 $\times 10^3$ J kg$^{-1}$.

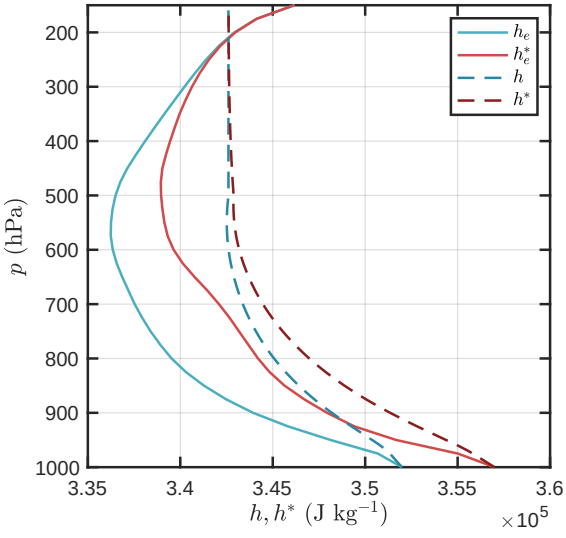


FIG. B2. Idealized profiles of $h_e$ (blue) $h_e^*$ (red), $h$ (blue dashed), $h^*$ (red dashed). The cloud cluster $h$ is obtained from Eq. (B7), $h^*$ is obtained by adding Eq (B9) to $h$. The environmental profiles $h_e$ and $h_e^*$ are idealized profiles based on sounding data from the DYNAMO northern sounding array (Yoneyama et al. 2013).

## APPENDIX C

### Plume buoyancy calculation

The calculation of the reanalysis-based $B_L$ shown in Fig. 9 closely follows Ahmed and Neelin (2018); Ahmed et al. (2020); Adames et al. (2021) and Vargas Martes et al. (2023). It is summarized here for completeness. If the mass flux in Eq. (B7) approximately increases linearly with height in the lower free troposphere, Eq. (B7) simplifies to the following:

$$h(p) = \frac{1}{p_0 - p} \int_{p_s}^{p} \frac{\partial M}{\partial p'} h_e dp' \tag{C1}$$

which states that the MSE of the plume at a pressure $p$ is equal to the average environment MSE of the layer beneath it. Note that we are now integrating in pressure rather than in height, and $p_0$ corresponds to the surface pressure. If we average $B$ from Eq. (42) over a lower troposphere layer ranging from 950-600 hPa we arrive at:

$$B_L = \frac{g}{C_p \kappa_L T_L} \left( w_B (h_B - h_L^*) - w_L (h_L^* - h_L) \right) \tag{C2}$$

where $w_B = 0.3$ and $w_L = 0.7$ are constants. The subscripts $_L$ and $_B$ denotes averaging over the 950-600 hPa and 1000-950 hPa layers, respectively.

### References


Adames, Á. F., 2022: The basic equations under weak temperature gradient balance: Formulation, scaling, and types of convectively coupled motions. *Journal of the Atmospheric Sciences*, **79 (8)**, 2087–2108.

Adames, Á. F., D. Kim, S. K. Clark, Y. Ming, and K. Inoue, 2019: Scale analysis of moist thermodynamics in a simple model and the relationship between moisture modes and gravity waves. *Journal of the Atmospheric Sciences*, doi:InPress.

Adames, Á. F., S. W. Powell, F. Ahmed, V. C. Mayta, and J. D. Neelin, 2021: Tropical precipitation evolution in a buoyancy-budget framework. *Journal of the Atmospheric Sciences*, **78 (2)**, 509 – 528, doi:10.1175/JAS-D-20-0074.1.

Ahmed, F., 2021: The mjo on the equatorial beta plane: An eastward-propagating rossby wave induced by meridional moisture advection. *Journal of the Atmospheric Sciences*, **78 (10)**, 3115–3135.

Ahmed, F., Á. Adames, and J. D. Neelin, 2020: Deep Convective Adjustment of Temperature and Moisture. *Journal of the Atmospheric Sciences*, **77 (6)**, 2163–2186, doi:10.1175/JAS-D-19-0227.1.

Ahmed, F., and J. D. Neelin, 2018: Reverse engineering the tropical precipitation–buoyancy relationship. *J. Atmos. Sci.*, **75 (5)**, 1587–1608, doi:10.1175/JAS-D-17-0333.1.

Ahmed, F., and J. D. Neelin, 2021: A process-oriented diagnostic to assess precipitation-thermodynamic relations and application to cmip6 models. *Geophysical Research Letters*, **48 (14)**, e2021GL094 108.

Ahmed, F., J. D. Neelin, and Á. F. Adames, 2021: Quasi-equilibrium and weak temperature gradient balances in an equatorial beta-plane model. *Journal of the Atmospheric Sciences*, **78 (1)**, 209 – 227, doi:10.1175/JAS-D-20-0184.1.

Arakawa, A., and W. H. Schubert, 1974: Interaction of a cumulus cloud ensemble with the large-scale environment, part i. *Journal of the Atmospheric Sciences*, **31 (3)**, 674–701, doi:10.1175/1520-0469(1974)031<0674:IOACCE>2.0.CO;2.

Back, L. E., Z. Hansen, and Z. Handlos, 2017: Estimating vertical motion profile top-heaviness: Reanalysis compared to satellite-based observations and stratiform rain fraction. *Journal of the Atmospheric Sciences*, **74 (3)**, 855–864.

Becker, T., C. S. Bretherton, C. Hohenegger, and B. Stevens, 2018: Estimating bulk entrainment with unaggregated and aggregated convection. *Geophysical Research Letters*, **45 (1)**, 455–462.

Becker, T., and C. Hohenegger, 2021: Entrainment and its dependency on environmental conditions and convective organization in convection-permitting simulations. *Monthly Weather Review*, **149 (2)**, 537–550.

Bischoff, T., and T. Schneider, 2014: Energetic constraints on the position of the intertropical convergence zone. *Journal of Climate*, **27 (13)**, 4937 – 4951, doi:10.1175/JCLI-D-13-00650.1, URL https://journals.ametsoc.org/view/journals/clim/27/13/jcli-d-13-00650.1.xml.

Blossey, P. N., C. S. Bretherton, and M. C. Wyant, 2009: Subtropical low cloud response to a warmer climate in a superparameterized climate model. part ii: Column modeling with a cloud resolving model. *Journal of Advances in Modeling Earth Systems*, **1 (3)**.

Bluestein, H., 1992: Synoptic-dynamic meteorology in midlatitudes: Volume 1, principles of kinematics and dynamics.

Bretherton, C. S., P. N. Blossey, and M. Khairoutdinov, 2005: An energy-balance analysis of deep convective self-aggregation above uniform SST. *J. Atmos. Sci.*, **62 (12)**, 4273–4292.

Bretherton, C. S., and P. K. Smolarkiewicz, 1989: Gravity Waves, Compensating Subsidence and Detrainment around Cumulus Clouds. *J. Atmos. Sci.*, **46 (6)**, 740–759, doi:10.1175/1520-0469(1989)046<0740:GWCSAD>2.0.CO;2.

Brown, R. G., and C. Zhang, 1997: Variability of midtropospheric moisture and its effect on cloud-top height distribution during toga coare*. *J. Atmos. Sci.*, **54 (23)**, 2760–2774, doi:10.1175/1520-0469(1997)054<2760:VOMMAI>2.0.CO;2.

Chang, C.-P., 1970: Westward propagating cloud patterns in the tropical pacific as seen from time-composite satellite photographs. *J. Atmos. Sci.*, **27 (1)**, 133–138, doi:10.1175/1520-0469(1970)027<0133:WPCPIT>2.0.CO;2.

Chang, C.-P., 1977: Viscous internal gravity waves and low–frequency oscillations in the tropics. *J. Atmos. Sci.*, **34 (6)**, 901–910, doi:10.1175/1520-0469(1977)034<0901:VIGWAL>2.0.CO;2.

Daleu, C. L., and Coauthors, 2015: Intercomparison of methods of coupling between convection and large-scale circulation: 1. comparison over uniform surface conditions. *Journal of Advances in Modeling Earth Systems*, **7 (4)**, 1576–1601.

Daleu, C. L., and Coauthors, 2016: Intercomparison of methods of coupling between convection and large-scale circulation: 2. comparison over nonuniform surface conditions. *Journal of Advances in Modeling Earth Systems*, **8 (1)**, 387–405.

De Rooy, W. C., and Coauthors, 2013: Entrainment and detrainment in cumulus convection: An overview. *Quarterly Journal of the Royal Meteorological Society*, **139 (670)**, 1–19.

de Szoeke, S. P., 2018: Variations of the moist static energy budget of the tropical indian ocean atmospheric boundary layer. *Journal of the Atmospheric Sciences*, **75 (5)**, 1545–1551, doi:10.1175/JAS-D-17-0345.1, URL https://doi.org/10.1175/JAS-D-17-0345.1.

Dias, J., M. Gehne, G. N. Kiladis, N. Sakaeda, P. Bechtold, and T. Haiden, 2018: Equatorial waves and the skill of ncep and ecmwf numerical weather prediction systems. *Monthly Weather Review*, **146 (6)**, 1763–1784.

Donner, L. J., and V. T. Phillips, 2003: Boundary layer control on convective available potential energy: Implications for cumulus parameterization. *Journal of Geophysical Research: Atmospheres*, **108 (D22)**, doi:10.1029/2003JD003773.

Duan, S. Q., F. Ahmed, and J. D. Neelin, 2024: Moist heatwaves intensified by entrainment of dry air that limits deep convection. *Nature Geoscience*, 1–8.

Edelman, A., and Coauthors, 2014: State of the tropics 2014 report.

Emanuel, K. A., J. David Neelin, and C. S. Bretherton, 1994: On large-scale circulations in convecting atmospheres. *Quarterly Journal of the Royal Meteorological Society*, **120 (519)**, 1111–1143, doi:10.1002/qj.49712051902.

Feng, Z., and S. Giangrande, 2018: Merged rwp-wacr-arscl cloud mask and cloud type. Atmospheric Radiation Measurement (ARM) Archive, Oak Ridge National Laboratory (ORNL), Oak Ridge, TN (US), doi:10.5439/1462693.

Gill, A. E., 1980: Some simple solutions for heat-induced tropical circulation. *Quart. J. Roy. Meteor. Soc.*, **106 (449)**, 447–462.

Gregory, D., J.-J. Morcrette, C. Jakob, A. Beljaars, and T. Stockdale, 2000: Revision of convection, radiation and cloud schemes in the ecmwf integrated forecasting system. *Quarterly Journal of the Royal Meteorological Society*, **126 (566)**, 1685–1710.

Hannah, W. M., 2017: Entrainment versus dilution in tropical deep convection. *Journal of the Atmospheric Sciences*, **74 (11)**, 3725–3747.

Held, I. M., R. S. Hemler, and V. Ramaswamy, 1993: Radiative-Convective Equilibrium with Explicit Two-Dimensional Moist Convection. *J. Atmos. Sci.*, **50 (23)**, 3909–3927.

Herman, M. J., and D. J. Raymond, 2014: Wtg cloud modeling with spectral decomposition of heating. *Journal of Advances in Modeling Earth Systems*, **6 (4)**, 1121–1140.

Hernandez-Duenas, G., L. M. Smith, and S. N. Stechmann, 2019: Weak-and strong-friction limits of parcel models: Comparisons and stochastic convective initiation time. *Quarterly Journal of the Royal Meteorological Society*, **145 (722)**, 2272–2291.

Houze, R. A., 2004: Mesoscale convective systems. *Reviews of Geophysics*, **42 (4)**, doi:10.1029/2004RG000150, URL https://agupubs.onlinelibrary.wiley.com/doi/abs/10.1029/2004RG000150.

Houze Jr, R. A., 1973: A climatological study of vertical transports by cumulus-scale convection. *Journal of Atmospheric Sciences*, **30 (6)**, 1112–1123.

Inoue, K., Á. F. Adames, and K. Yasunaga, 2020: Vertical Velocity Profiles in Convectively Coupled Equatorial Waves and MJO: New Diagnoses of Vertical Velocity Profiles in the Wavenumber–Frequency Domain. *Journal of the Atmospheric Sciences*, **77 (6)**, 2139–2162, doi:10.1175/JAS-D-19-0209.1.

Janiga, M. A., C. J. Schreck, J. A. Ridout, M. Flatau, N. P. Barton, E. J. Metzger, and C. A. Reynolds, 2018: Subseasonal forecasts of convectively coupled equatorial waves and the mjo: Activity and predictive skill. *Monthly Weather Review*, **146 (8)**, 2337–2360.

Kim, H., F. Vitart, and D. E. Waliser, 2018: Prediction of the madden–julian oscillation: A review. *Journal of Climate*, **31 (23)**, 9425–9443, doi:10.1175/JCLI-D-18-0210.1.

Kim, J.-E., and C. Zhang, 2021: Core dynamics of the mjo. *Journal of the Atmospheric Sciences*, **78 (1)**, 229–248.

Kingsmill, D. E., and R. A. Houze, Jr, 1999: Thermodynamic characteristics of air flowing into and out of precipitating convection over the west pacific warm pool. *Quarterly Journal of the Royal Meteorological Society*, **125 (556)**, 1209–1229, doi:10.1002/qj.1999.49712555606, URL https://rmets.onlinelibrary.wiley.com/doi/abs/10.1002/qj.1999.49712555606.

Kuang, Z., 2008: A Moisture-Stratiform Instability for Convectively Coupled Waves. *J. Atmos. Sci.*, **65 (3)**, 834–854.

Kuang, Z., 2011: The wavelength dependence of the gross moist stability and the scale selection in the instability of column-integrated moist static energy. *J. Atmos. Sci.*, **68 (1)**, 61–74.

Kuo, Y.-H., and J. D. Neelin, 2022: Conditions for convective deep inflow. *Geophysical Research Letters*, **49 (20)**, e2022GL100 552.

Lin, J.-L., B. E. Mapes, and W. Han, 2008: What are the sources of mechanical damping in matsuno–gill-type models? *Journal of Climate*, **21 (2)**, 165–179.

Lin, J.-L., M. Zhang, and B. Mapes, 2005: Zonal Momentum Budget of the Madden-Julian Oscillation: The Source and Strength of Equivalent Linear Damping. *J. Atmos. Sci.*, **62 (7)**, 2172–2188.

Lucas, C., E. J. Zipser, and M. A. Lemone, 1994: Vertical velocity in oceanic convection off tropical australia. *Journal of the Atmospheric Sciences*, **51 (21)**, 3183–3193, doi:10.1175/1520-0469(1994)051<3183:VVIOCO>2.0.CO;2.

Majda, A. J., and S. N. Stechmann, 2008: Stochastic models for convective momentum transport. *Proceedings of the National Academy of Sciences*, **105 (46)**, 17 614–17 619.

Mapes, B. E., 1993: Gregarious tropical convection. *Journal of the Atmospheric Sciences*, **50 (13)**, 2026–2037, doi:10.1175/1520-0469(1993)050<2026:GTC>2.0.CO;2.

Mapes, B. E., and X. Wu, 2001: Notes and correspondence convective eddy momentum tendencies in long cloud-resolving model simulations. *Journal of the atmospheric sciences*, **58 (5)**, 517–526.

Moorthi, S., and M. J. Suarez, 1992: Relaxed arakawa-schubert. a parameterization of moist convection for general circulation models. *Monthly Weather Review*, **120 (6)**, 978–1002.

Muller, C., and Coauthors, 2022: Spontaneous aggregation of convective storms. *Annual Review of Fluid Mechanics*, **54 (1)**, 133–157.

Nicholls, M. E., R. A. Pielke, and W. R. Cotton, 1991: Thermally forced gravity waves in an atmosphere at rest. *Journal of the Atmospheric Sciences*, **48 (16)**, 1869–1884, doi:10.1175/1520-0469(1991)048<1869:TFGWIA>2.0.CO;2.

Raymond, D., Ž. Fuchs, S. Gjorgjievska, and S. Sessions, 2015: Balanced dynamics and convection in the tropical troposphere. *J. Adv. Model. Earth Syst.*, **7**, 1093–1116, doi:10.1002/2015MS000467.

Raymond, D. J., 1994: Cumulus convection and the madden-julian oscillation of the tropical troposphere. *Physica D: Nonlinear Phenomena*, **77 (1)**, 1 – 22, doi:https://doi.org/10.1016/0167-2789(94)90124-4, URL http://www.sciencedirect.com/science/article/pii/0167278994901244, special Issue Originating from the 13th Annual International Conference of the Center for Nonlinear Studies Los Alamos, NM, USA, 21 May 1993.

Romps, D. M., 2010: A direct measure of entrainment. *Journal of the Atmospheric Sciences*, **67 (6)**, 1908–1927.

Romps, D. M., 2012a: Numerical tests of the weak pressure gradient approximation. *Journal of the atmospheric sciences*, **69 (9)**, 2846–2856.

Romps, D. M., 2012b: Weak pressure gradient approximation and its analytical solutions. *Journal of the Atmospheric Sciences*, **69 (9)**, 2835–2845.

Romps, D. M., 2014: Rayleigh damping in the free troposphere. *J. Atmos. Sci.*, **71 (2)**, 553–565.

Romps, D. M., 2021: Ascending columns, wtg, and convective aggregation. *Journal of the Atmospheric Sciences*, **78 (2)**, 497–508.

Ruppert, J. H., and C. Hohenegger, 2018: Diurnal circulation adjustment and organized deep convection. *Journal of Climate*, **31 (12)**, 4899–4916, doi:10.1175/JCLI-D-17-0693.1.

Schiro, K. A., F. Ahmed, S. E. Giangrande, and J. D. Neelin, 2018: Goamazon2014/5 campaign points to deep-inflow approach to deep convection across scales. *Proceedings of the National Academy of Sciences*, **115 (18)**, 4577–4582, doi:10.1073/pnas.1719842115, URL https://www.pnas.org/content/115/18/4577, https://www.pnas.org/content/115/18/4577.full.pdf.

Schiro, K. A., and J. D. Neelin, 2019a: Deep convective organization, moisture vertical structure, and convective transition using deep-inflow mixing. *Journal of the Atmospheric Sciences*, **76 (4)**, 965–987.

Schiro, K. A., and J. D. Neelin, 2019b: Deep convective organization, moisture vertical structure, and convective transition using deep-inflow mixing. *Journal of the Atmospheric Sciences*, **76 (4)**, 965–987, doi:10.1175/JAS-D-18-0122.1.

Schiro, K. A., J. D. Neelin, D. K. Adams, and B. R. Lintner, 2016: Deep convection and column water vapor over tropical land versus tropical ocean: A comparison between the amazon and the tropical western pacific. *Journal of the Atmospheric Sciences*, **73 (10)**, 4043–4063.

Schiro, K. A., S. C. Sullivan, Y.-H. Kuo, H. Su, P. Gentine, G. S. Elsaesser, J. H. Jiang, and J. D. Neelin, 2020: Environmental controls on tropical mesoscale convective system precipitation intensity. *Journal of the Atmospheric Sciences*, **77 (12)**, 4233–4249.

Schumacher, C., R. A. Houze, and I. Kraucunas, 2004: The Tropical Dynamical Response to Latent Heating Estimates Derived from the TRMM Precipitation Radar. *J. Atmos. Sci.*, **61**, 1341–1358.

Schumacher, C., S. N. Stevenson, and C. R. Williams, 2015: Vertical motions of the tropical convective cloud spectrum over darwin, australia. *Quarterly Journal of the Royal Meteorological Society*, **141 (691)**, 2277–2288.

Sessions, S. L., S. Sentić, and D. J. Raymond, 2019: Balanced dynamics and moisture quasi-equilibrium in dynamo convection. *Journal of the Atmospheric Sciences*, **76 (9)**, 2781–2799.

Singh, M. S., and S. Neogi, 2022: On the interaction between moist convection and large-scale ascent in the tropics. *Journal of Climate*, 1–47.

Singh, M. S., and P. A. O'Gorman, 2013: Influence of entrainment on the thermal stratification in simulations of radiative-convective equilibrium. *Geophysical Research Letters*, **40 (16)**, 4398–4403, doi: 10.1002/grl.50796.

Singh, M. S., R. A. Warren, and C. Jakob, 2019: A steady-state model for the relationship between humidity, instability, and precipitation in the tropics. *Journal of Advances in Modeling Earth Systems*, **11 (12)**, 3973–3994.

Sobel, A. H., and C. S. Bretherton, 2000: Modeling Tropical Precipitation in a Single Column. *J. Climate*, **13**, 4378–4392.

Sobel, A. H., J. Nilsson, and L. M. Polvani, 2001: The Weak Temperature Gradient Approximation and Balanced Tropical Moisture Waves. *J. Atmos. Sci.*, **58**, 3650–3665.

Tung, W.-w., C. Lin, B. Chen, M. Yanai, and A. Arakawa, 1999: Basic modes of cumulus heating and drying observed during toga-coare iop. *Geophysical research letters*, **26 (20)**, 3117–3120.

Tung, W.-W., and M. Yanai, 2002: Convective momentum transport observed during the toga coare iop. part i: General features. *Journal of the atmospheric sciences*, **59 (11)**, 1857–1871.

Vargas Martes, R. M., Á. F. Adames Corraliza, and V. C. Mayta, 2023: The role of water vapor and temperature in the thermodynamics of tropical northeast pacific and african easterly waves. *Journal of the Atmospheric Sciences*, **80 (9)**, 2305–2322.

Wang, S., A. H. Sobel, and Z. Kuang, 2013: Cloud-resolving simulation of toga-coare using parameterized large-scale dynamics. *Journal of Geophysical Research: Atmospheres*, **118 (12)**, 6290–6301.

Weisman, M. L., and J. B. Klemp, 1986: Characteristics of isolated convective storms. *Mesoscale meteorology and forecasting*, Springer, 331–358.

Wing, A. A., K. Emanuel, C. E. Holloway, and C. Muller, 2018: Convective self-aggregation in numerical simulations: A review. *Shallow clouds, water vapor, circulation, and climate sensitivity*, 1–25.

Wing, A. A., and K. A. Emanuel, 2014: Physical mechanisms controlling self-aggregation of convection in idealized numerical modeling simulations. *J. Adv. Model. Earth Syst.*, **6 (1)**, 59–74.

Wolding, B., S. W. Powell, F. Ahmed, J. Dias, M. Gehne, G. Kiladis, and J. D. Neelin, 2022: Tropical thermodynamic–convection coupling in observations and reanalyses. *Journal of the Atmospheric Sciences*, **79 (7)**, 1781–1803.

Xu, X., C. Sun, C. Lu, Y. Liu, G. J. Zhang, and Q. Chen, 2021: Factors affecting entrainment rate in deep convective clouds and parameterizations. *Journal of Geophysical Research: Atmospheres*, **126 (15)**, e2021JD034 881.

Yanai, M., S. Esbensen, and J. Chu, 1973: Determination of bulk properties of tropical cloud clusters from large-scale heat and moisture budgets. *J. Atmos. Sci.*, **30**, 611–627, doi:10.1175/1520-0469(1973)030<0611:DOBPOT>2.0.CO;2.

Yang, D., 2019: Convective heating leads to self-aggregation by generating available potential energy. *Geophysical Research Letters*, **46 (17-18)**, 10 687–10 696.

Yano, J.-I., and R. Plant, 2012: Convective quasi-equilibrium. *Reviews of Geophysics*, **50 (4)**.

Yoneyama, K., C. Zhang, and C. N. Long, 2013: Tracking Pulses of the Madden–Julian Oscillation. *Bulletin of the American Meteorological Society*, **94 (12)**, 1871–1891.

Zangvil, A., 1975: Temporal and spatial behavior of large-scale disturbances in tropical cloudiness deduced from satellite brightness data. *Monthly Weather Review*, **103 (10)**, 904–920.

Zhang, G. J., and N. A. McFarlane, 1995a: Role of convective scale momentum transport in climate simulation. *J. Geophys. Res.*, **100**, 1417–1426.

Zhang, G. J., and N. A. McFarlane, 1995b: Sensitivity of climate simulations to the parameterization of cumulus convection in the canadian climate centre general circulation model. *Atmosphere-ocean*, **33 (3)**, 407–446.